Optimal Spin Control in Nitrogen Vacancy Centers in Diamond

A Thesis

submitted to the
Indian Institute of Science Education and Research, Pune
in partial fulfillment of the requirements for the
BS-MS Dual Degree Programme

Rounak Jha

Indian Institute of Science Education and Research Pune
Dr. Homi Bhabha Road,
Pashan, Pune 411008, INDIA.

01 June, 2021

Supervisor: Prof. Dieter Suter

Certificate

This is to certify that this dissertation, entitled 'Optimal Spin Control in Nitrogen Vacancy Centers in Diamond', submitted towards the partial fulfillment of the requirements of the BS-MS dual degree programme at the Indian Institute of Science Education and Research, Pune represents study/work carried out by Rounak Jha at Technische Universität Dortmund, under the supervision of Prof. Dieter Suter, Professor of Physics, Technische Universität Dortmund during the academic year 2020-2021.

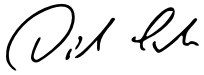

Prof. Dieter Suter

Thesis Advisory Committee:

Prof. Dieter Suter

Prof. T.S. Mahesh

This thesis is dedicated to Tatu, for being my perpetual source of support, and Aanj, for constantly pushing me to be the best version of myself.

Declaration

I hereby declare that the matter embodied in the report entitled "Optimal Spin Control in Nitrogen Vacancy Centers in Diamond ", is the result of the work carried out by me at Technische Universität Dortmund, under the supervision of Prof. Dieter Suter and the same has not been submitted elsewhere for any other degree.

Rounak Jha

Acknowledgments

I would like to thank Prof. Dieter Suter for giving me the opportunity to conduct research in this exciting field and for his unparalleled guidance and support, especially at a time when I had to initially start my project remotely. I am certain that the skills and traits that I have learnt in my project will help me in the next stage of my research. I would like to thank Swathi, Yihua, Jingfu, Vincent and Harpreet for their help and guidance during this project. I would also like to thank Prof. Fedor Jelezko, for taking out the time to mentor me through remote interactions throughout this project, at a time when travel to Ulm University wasn't possible. I am extremely grateful to Prof. T.S Mahesh for his constant guidance and support as my mentor over the last three years, and for giving me the freedom to explore this wonderful field. I am also thankful to Rupak, Priya and Soham for the insightful discussions during this project. I would also like to thank Prof. Panigrahi for his support ever since my very first research project with him in the summer of 2018.

I would like to thank Sandhya, Avinash and Pronoy for constantly being there with their wonderful little quirks to provide the laughs when things got stressful, and the support when I needed it. I am eternally grateful to my friends at IISER Pune for making this journey so wonderful - Adarsh, Onkar, Adithya, Harshavardhan, Mohan, Appu, Rohit, Akhila, Suman, Vishal, Sanjana, Devadarshini, Mansi and so many others. These 5 years have been some of the best of my life so far, and I have them to thank for it.

I also owe my heartfelt gratitude to Aanjaneya, for being there as a perennial source of support during my time at IISER, through good times and bad. The tough love he has provided has ensured that I set higher standards for myself, both as a researcher and a person. Despite being an only child all my life, I was never allowed the chance to feel any remorse over the lack of a sibling. The love and support I have received from Anwesh before and during my time at IISER render the word 'cousin' meaningless. From staying up till 5am

to help me write applications to fighting over who gets the last piece of nadu, his bumbling presence has always been reassuring.

I am grateful for all the love I have received in this lifetime by my Didu and late Thamma. I want to thank my father, who supported me throughout this journey, and was there whenever I needed his advice. Finally, I want to thank my mother for her love and encouragement at every step of the way, and for her steadfast belief in me, even when I doubted myself. I owe everything that I am today to her.

Abstract

In this thesis, we explore the effect of single qubit (electron) control techniques like Rabi oscillations, Free Induction Decay (FID) and Dynamical Decoupling (DD), using microwave (MW) pulse sequences. We characterize the Hamiltonian of both single and two-qubit systems and simulate the effect of these pulse sequences, before verifying these effects experimentally. We also talk about the quantum state tomography (QST) of a single qubit in NV centers. Next, we move on to nuclear spin control using radio-frequency (RF) and MW pulse sequences, and obtain nuclear spin Rabi oscillations and FID. Finally, we talk some of the challenges associated with the experimental implementation of these techniques, before exploring a method to counter one of these challenges.

The successful implementation of these techniques opens up the road to using more advanced pulse sequences on both single (electron spin) and multiple (electron with nuclear spin) qubit systems for achieving required gate operations, as well as protecting spins from decoherence due to interactions with the environment.

Contents

List of Figures

Chapter 1

Introduction

1.1 The Nitrogen Vacancy (NV) center

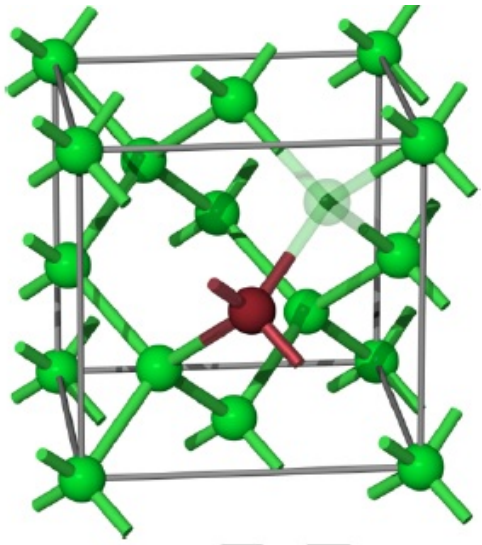

Figure 1.1: The NV center. The red atom is the substitutional ^{14}N while the green ones are the carbon atoms [1].

Diamonds have many kinds of defects present, some of which exhibit strong optical transitions and lie within the band-gap of diamond. One of the most common defects is the presence of a substitutional nitrogen, or 'P1' center, which gives the diamond a yellowish colour at high concentrations. In some cases, one of the sites where a carbon atom is

substituted by this nitrogen atom also has a vacancy, i.e one of its four neighbours is missing [1]. The lone pair of electrons of the nitrogen points towards the vacancy, and the three dangling carbon bonds each contribute an electron to the vacancy. Such a site constitutes a NV center (Fig 1.1).

There are two types of NV centers - neutral or NV^0 and negative or NV^- centers. The NV^0 centers have a total of five electrons - two from the lone pair of the ^{14}N and one each from the three C atoms located next to the vacancy - and thus form a spin $S = \frac{1}{2}$ system. Sometimes these centers contain an extra electron (NV^-) to have a total of 6 electrons and form a spin $S = 1$ system. We perform all our experiments on NV^- centers, which have a strong optical transition between the ground and excited states.

Nitrogen Vacancy (NV) centers in diamonds were first identified in the 1970s, and since then have paved the way for tremendous progress in a multitude of fields. Not only do they serve as a highly useful platform for research in quantum computing and information processing, they also have diverse applications in the fields of sensing, imaging, nanophotonics and ultrafast spectroscopy, among others. Owing to their multifaceted nature, they have the potential to drive interdisciplinary research in the future.

NV centers have emerged as one of the most promising contenders for quantum computers, as they have relatively long lived quantum states with well defined optical transitions [1, 2]. The presence of different types of qubits in the form of electron and nuclear spins has promoted the use of NV centers as hybrid quantum registers. The difference in the inherent properties of the spins allow them to be used for both fast gate operations and long term information storage. Solving the challenges associated with trying to protect the electron spin in order to retain memory storage and also performing fast gate operations on nuclear spins form an integral area of current research.

We discuss the theoretical effects and experimental implementation of various spin control techniques, for both the electron as well as the ^{14}N nuclear spin.

Chapter 2

Hamiltonian Characterization of an NV center

2.1 The static Hamiltonian

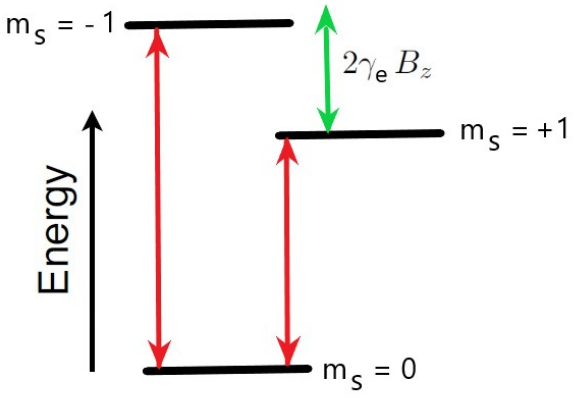

Figure 2.1: The energy level diagram of the electron spin system [1].

For single qubit experiments, we consider only the electron spin ($S = 1$) of the NV center, not coupled to any nuclear spins. Such a system is characterized by the lab-frame static Hamiltonian [3]:

$$\frac{H_{static}}{2\pi} = DS_z^2 - h\gamma_e B_{0z} S_z = DS_z^2 - h\nu_0 S_z \tag{2.1}$$

where $S_z = \frac{\sigma_z}{2}$ (σ_z is the 2 dimensional z Pauli matrix) is the electron spin angular momentum operator, B_{0z} is the static magnetic field along the z axis, $D = 2.87$ GHz is the zero field splitting, $\gamma_e = 28$ GHz/T is the gyromagnetic ratio of the electron spin and ν_0 is the Larmor (spin) frequency. The equation (2.1) is called the static Hamiltonian as it is applied through a static magnetic field. An important point to note here is that the z axis is chosen as the NV axis or symmetry axis of the center. For the rest of this thesis, all Hamiltonians of the form $\frac{H}{2\pi}$ will simply be written as H, and the value of h will be taken as 1 for convenience.

The energy level diagram of the ground state triplet of the electron spin qubit is shown in Figure 2.1. The frequency difference between the frequencies of the two transitions $m_s = 0$ to $m_s = +1$ and $m_s = 0$ to $m_s =$ -1 is 2 $\gamma_e B_{0z} S_z$. The frequencies corresponding to these transitions are determined through a process called optically detected magnetic resonance (ODMR) For our electron spin control experiments, we select one of these two transition frequencies, and thus restrict ourselves to the two-dimensional subspace of the 3 dimensional Hilbert space of a spin $S = 1$ electron.

2.2 The control Hamiltonian

The control Hamiltonian is applied in the form of a control magnetic field of amplitude B_1(t) applied in the x-y plane, whose magnitude oscillates with a carrier frequency ν_{mw}, which is at or near the spin frequency ν_0. The control Hamiltonian in the lab frame is:

$$H_{mw} = -2\gamma_e B_1 \cos(\nu_{mw} t + \phi) S_x = -2\nu_1 \cos(\nu_{mw} t + \phi) S_x \tag{2.2}$$

where the spin operators $S_x = \frac{\sigma_x}{2}$ and $S_y = \frac{\sigma_y}{2}$ (σ_x and σ_y are the 2 dimensional x and y Pauli matrices respectively). B_1 and ϕ, the amplitude and phase of the MW field respectively, can both be varied to achieve the required operation, and ν_1 is the Rabi frequency.

Thus, the total Hamiltonian in the lab frame is:

$$H_{lab} = DS_z^2 - \gamma_e B_{0z} S_z - 2\gamma_e B_1 \cos(\nu_{mw} t + \phi) S_x \tag{2.3}$$

2.3 The rotating frame

Calculating the motion of an electron spin under the influence of an static and alternating magnetic field is difficult to do in the lab frame. Moving to a frame rotating about the z axis at a frequency ν_{mw} (the rotating frame) results in a much simpler calculation. The state in the lab frame $|\psi\rangle$ transforms to $|\psi_{rot}\rangle$ in the rotating frame as:

$$|\psi\rangle_{rot} = exp(-i\nu_{mw} t S_z) |\psi\rangle . \tag{2.4}$$

When we substitute the lab frame $|\psi\rangle$ in the Schrodinger's equation ($i(\frac{d}{dt}|\psi\rangle) = H_{lab}|\psi\rangle$) with the above Hamiltonian, it gives ($i(\frac{d}{dt}|\psi\rangle_{rot}) = H_{rot}|\psi\rangle$), with:

$$H_{rot} = DS_z^2 - (\nu_0 - \nu_{mw}) S_z - \nu_1 [\cos\phi S_x - \sin\phi S_y]. \tag{2.5}$$

Equation (2.5) is the result of an approximation known as the rotating wave approximation, detailed in Section 2.3.1.

The rotating frame Hamiltonian is used for simulating the effect of various pulse sequences in the following chapters.

2.3.1 Proof of Equation 2.5

According to the Schrodinger equation:

$i(\frac{d}{dt}|\psi\rangle) = H_{lab}|\psi\rangle$

$\implies i(\frac{d}{dt}(\exp(i\nu_{mw} t S_z)|\psi\rangle_{rot}) = H_{lab}(\exp(i\nu_{mw} t S_z)|\psi\rangle_{rot})$

$\implies i(\exp(i\nu_{mw} t S_z)\frac{d}{dt}|\psi\rangle_{rot} + i\nu_{mw} S_z(\exp(i\nu_{mw} t S_z)|\psi\rangle_{rot}))$

$= H_{lab}(\exp(i\nu_{mw}tS_z)\left|\psi\right\rangle_{rot})$

$\implies i(\frac{d}{dt}\left|\psi\right\rangle_{rot} + i\nu_{mw}S_z\left|\psi\right\rangle_{rot}) = \exp(-i\nu_{mw}tS_z)H_{lab}(\exp(i\nu_{mw}tS_z)\left|\psi\right\rangle_{rot})$

$\implies \frac{d}{dt}\left|\psi\right\rangle_{rot} = -i(\exp(-i\nu_{mw}tS_z)H_{lab}(\exp(i\nu_{mw}tS_z)\left|\psi\right\rangle_{rot}) - i\nu_{mw}S_z\left|\psi\right\rangle_{rot}$

$\implies \frac{d}{dt}\left|\psi\right\rangle_{rot} = -iH_{rot}\left|\psi\right\rangle_{rot}$; where $H_{rot} = \exp(-i\nu_{mw}tS_z)H\exp(i\nu_{mw}tS_z) + \nu_{mw}S_z$

For the static part of the Hamiltonian in the lab frame: $H_{static} = DS_z^2 - \gamma_e B_0 S_z = DS_z^2 - \nu_0 S_z$.

Let H'_{static} and H'_{mw} be the static and control Hamiltonian in the rotating frame respectively.

$\implies H'_{static} = \exp(-i\nu_{mw}tS_z)H_{static}\exp(i\nu_{mw}tS_z) + \nu_{mw}S_z$

Since S_z commutes with itself, $H'_{static} = H_{static} + \nu_{mw}S_z = DS_z^2 - (\nu_0 - \nu_{mw})S_z$

For the control Hamiltonian in the lab frame: $H_{mw} = -2\nu_1[\cos(\nu_{mw}t + \phi)S_x]$, and

$H'_{mw} = \exp(-i\nu_{mw}tS_z)H_{mw}\exp(i\nu_{mw}tS_z)$

$\implies H'_{mw} = -2\nu_1\cos(\nu_{mw}t + \phi)[\exp(-i\nu_{mw}tS_z)S_x\exp(i\nu_{mw}tS_z)]$.

According to the sandwich formula [11], if the operators A, B and C cyclically commute:

$\exp(-i\theta A)B\exp(i\theta A) = B\cos\theta + C\sin\theta$

If we take $S_z = A$ and $S_x = B$, then according to the cyclical commutation property, we get $S_y = C$.

Using this formula, with $\theta = \nu_{mw}t$, we get:

$H'_{mw} = -2\nu_1\cos(\nu_{mw}t + \phi)[\cos(\nu_{mw}t)S_x + \sin(\nu_{mw}t)S_y]$

$\implies H'_{mw} = -\nu_1[2\cos(\nu_{mw}t + \phi)\cos(\nu_{mw}t)S_x + 2\cos(\nu_{mw}t + \phi)\sin(\nu_{mw}t)S_y]$

$\implies H'_{mw} = -\nu_1\{[\cos(2\nu_{mw}t + \phi) + \cos(\phi)]S_x + [\sin(2\nu_{mw}t + \phi) - \sin(\phi)]S_y\}$

Here, we apply the rotating wave approximation [4], which says that if the electromagnetic radiation is near resonance with an atomic transition, we can ignore the terms that oscillate

at a higher frequency, and keep the terms oscillating at a lower frequency. Here, since ν_{mw} is near resonance with ν_0, we can ignore the term $\cos(2\nu_{mw}t+\phi)$ with respect to $\cos(\phi)$, and similarly ignore the term $\sin(2\nu_{mw}t+\phi)$ with respect to $\sin(\phi)$. Finally, we get:

$H'_{mw} = -\nu_1[\cos\phi S_x - \sin\phi S_y]$.

Thus, the rotating frame Hamiltonian is:

$H_{rot} = H'_{static} + H'_{mw} = DS_z^2 - (\nu_0 - \nu_{mw})S_z - \nu_1[\cos\phi S_x - \sin\phi S_y]$.

2.4 Two spin system

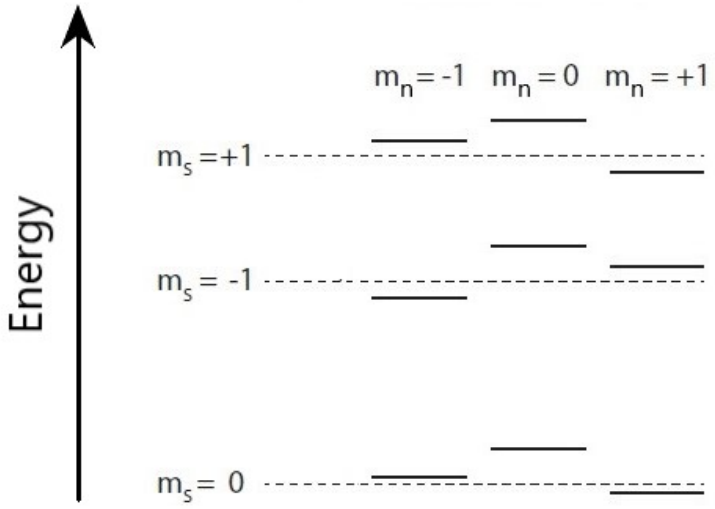

Figure 2.2: The energy level diagram of the two spin electron and ^{14}N system [5].

Although we perform MW pulse operations only on the electron spin, we need to consider that the electron spin is also coupled to nuclear spins, such as the ^{14}N spin. The static Hamiltonian for such a system in the lab frame is:

$$H_{2static} = -\gamma_e B_{0z} S_{2/3z} - \gamma_n B_{0z} I_{2/3z} + DS_{2/3z}^2 + PI_{2/3z}^2 + A_{\parallel} S_{2/3z} I_{2/3z} \tag{2.6}$$

where γ_e = -28 GHz/T is the gyromagnetic ratio of the electron, γ_n = 3.1MHz/T is the gyromagnetic ratio of the nucleus, D = 2.87 GHz is the zero field splitting, P = -4.95

MHz is the nuclear quadrupolar splitting, $A_{\|}$ = -2.16 MHz is the secular component of the hyperfine coupling between the electron and nuclear spin (the non-secular components have been ignored here) and $S_{2/3z}$ and $I_{2/3z}$ are the electron and nuclear spin angular momentum operators in the 4 dimensional (S_{2z} and I_{2z}) or 6 dimensional (S_{3z} and I_{3z}) subspace of the 9 dimensional Hilbert space (i.e the 9×9 density matrix formed by a system consisting of two spin $S = 1$ particles) respectively, depending on whether the nuclear spin is a qubit ($S = \frac{1}{2}$) or a qutrit ($S = 1$). ($S_{2z} = S_z \otimes I_2$ and $I_{2z} = I_z \otimes I_2$, where I_2 is the two dimensional identity matrix, while $S_{3z} = S_z \otimes I_3$ and $I_{3z} = I_z \otimes I_3$, where I_3 is the three dimensional identity matrix).

The complete energy level diagram for a two spin system (with the electron spin qutrit and the nuclear spin qutrit) is shown in Figure 2.2.

Since for MW experiments, the control fields only affect the electron spin and not the nuclear spin, the control field Hamiltonian in the lab frame is written as:

$$H_{2mw} = -2\gamma_e B_1 \cos(\nu_{mw} t + \phi) S_{2/3x} \tag{2.7}$$

where $S_{2/3x}$ and $S_{2/3y}$ are the electron spin angular momentum operators in the 4/6 dimensional subspace of the 9 dimensional Hilbert space ($S_{2x} = S_x \otimes I_2$, $S_{3x} = S_x \otimes I_3$, $S_{2y} = S_y \otimes I_2$ and $S_{3y} = S_y \otimes I_3$).

On similarly transforming this Hamiltonian to a frame rotating at a frequency ν_{mw} w.r.t the electron spin, we get:

$$H_{2rot} = -(\nu_0 - \nu_{mw}) S_{2/3z} - \nu_1 [\cos\phi S_{2/3x} - \sin\phi S_{2/3y}] + D S_{2/3z}^2 + P I_{2/3z}^2 + A_{\|} S_{2/3z} I_{2/3z}. \tag{2.8}$$

For two qubit and nuclear spin experiments performed in this thesis, we only consider ^{14}N as the nuclear spin.

Note: In all future chapters, the durations of all MW pulses (except transition selective pulses) are assumed to be short enough that we can ignore the effect of the hyperfine coupling during the application of the pulses.

Chapter 3

The setup

In this chapter, I briefly explain the details of the layout of the NV setup, as well as the functions of each component.

3.1 Setup components

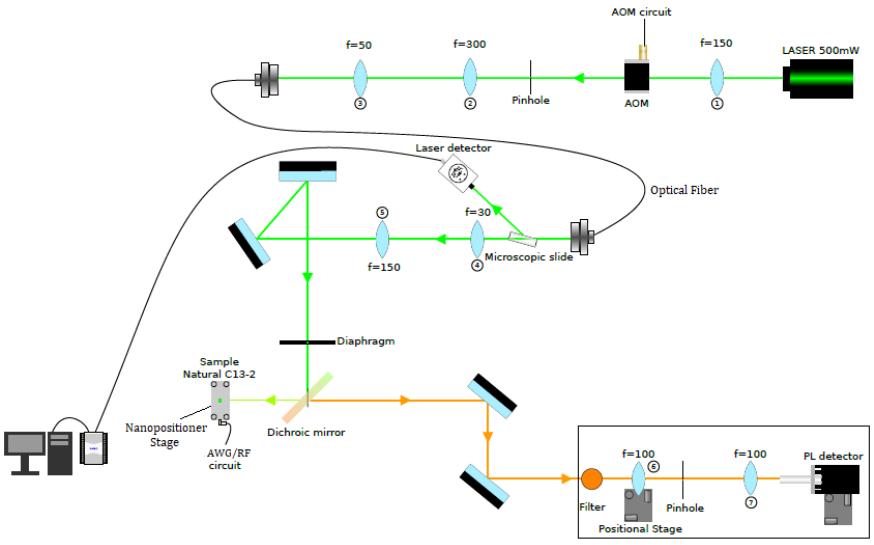

Figure 3.1: A schematic of the NV center setup [6].

A schematic of one of the NV setups present in the lab is shown in Figure 3.1. The

different components present in the setup are:

1. Laser: Used as a coherent light source to perform optical experiments. A green laser beam of wavelength 532 nm is used for our experiments.

2. Lenses: Used for focusing and collimation of the laser beam. The focal length (in mm) of the lenses is shown in Figure 3.1.

3. Pinholes: Used to allow only a certain portion of the laser beam to pass through, and block the rest. In combination with the AOM, it allows only the first order diffraction of the laser beam to pass through.

4. Mirrors: Used to reflect and align the path of the beam.

5. Optical fiber: Used to give the beam a Gaussian profile. The NV setup used for this experiment has a 'single-mode' optical fiber.

6. Laser detector: Used to measure the power of the laser beam exiting the fiber (to calculate the loss of signal), and to confirm whether the beam is reaching the sample.

7. Microscope slide: The microscope slide is used to reflect and transmit the laser beam each partially (90 % transmission and 10 % reflection). Used in conjunction with a photodetector to confirm that the transmitted beam is reaching the sample.

8. AWG (Arbitrary Waveform Generator): Used to generate the shaped MW pulses (or pulse sequences) that are used in QIP experiments.

9. Dichroic Mirror: A mirror which allows the visible beam from the laser beam to get reflected and enter the sample, and subsequently allows the light emitted by the particular NV center of the sample (photoluminescence) to be transmitted through it and eventually get focused on to the PL detector. The dichroic mirror used in our NV setup is a 594 nm long pass one, which means that it only transmits light having a wavelength of above 594 nm, and thus prevents the green light from the initial laser beam from passing through it.

10. PL detector: Used to measure the light scattered by the NV center sample (Time Correlated Single Photon Counting module).

11. Longpass filter: Used to allow only the light beyond the mentioned wavelength to

pass through.

12. Amplifiers and attenuators: Used to amplify and dampen the signal power respectively. Used in the AOM circuit (not shown in figure).

13. Electromagnet 2 axis motor controller: Used to control the orientation of the magnetic field, optimizing the field orientation for a particular center.

14. Nanoposition system: The stage on which the objective lens (used to irradiate the sample with the laser) is placed. Moving the nanopositioner moves the objective lens and determines which portion of the sample gets irradiated.

15. Sample: The diamond sample containing the NV centers, arguably the most important part of the setup!

16. Copper wire: Used to apply the control magnetic field on the sample, thus enabling us to perform spin control experiments.

17. RF signal generator: To generate the RF pulses used for controlling the nuclear spin directly, and perform nuclear spin experiments.

18. Acousto-Optic Modulator (AOM): A device used to modulate the power of the laser beam. It consists of a piezoelectric transducer attached to a material like glass. When an oscilating electric signal is applied by the Voltage controlled oscillator (VCO), it causes the transducer to vibrate and creates sound waves in the material. These sound waves diffract the laser beam, and the intensity of the sound wave decides the amount of light diffracted. Hence, the intensity of light in the diffracted beam can be modulated by the intensity of the sound wave. The Voltage Variable Attenuator (VVA) is used to vary the power of the signal reaching the AOM, as it provides an attenuation that varies with the voltage.

3.2 Path travelled by the beam

The laser sends a beam of the specified wavelength. This beam is then focused onto the AOM, which is used to modulate the power of the beam. Next, the beam passes through a pinhole, which ensures only the first order diffraction of the laser beam is allowed to pass

through. The beam is then focused on to the single-mode optical fiber, where it gains a Gaussian profile. The beam coming out of the optical fiber is diverging, so it is collimated with the help of two lenses. The NV setup also has a portion of the beam reflected to a laser detector (using a microscope slide) to measure the intensity of the laser coming out of the fiber, and ensure that the beam is reaching the sample. The rest of the beam moves on to a dichroic mirror, from which it is reflected on to the sample. The NV centers in the sample absorb the light of this wavelength and go to their excited state, before jumping back to the ground state and emitting a photon. The emitted light is then transmitted through the dichroic mirror, and after passing through the long-pass filter (used to ensure that no green light passes through as well), the light is focused using a lens and then passes through a pinhole. The pinhole ensures that only the photoluminescence from the measured NV center is considered, and neighbouring NV centers do not contribute. Finally, the light is focused on to the PL detector (using another lens), where the photoluminescence is measured. Most of the setup components, as well as the path of the beam are shown in Figure 3.1.

3.3 Setup problems worked on

3.3.1 Optical alignment

We worked on the optical alignment of the setup in order to increase the number of scattered photons (and thus the photoluminescence) detected by the PL detector. This was done to ensure the proper detection of the vacancy centers, through a better contrast. The images of the scans before and after the optical alignment are shown in Figure 3.2. The scan before the alignment has a maximum photoluminescence count of 33k photons per second, while the scan after the alignment has a maximum photoluminescence count of 61k photons per second (for the same scan duration), and a much better contrast. This was an imperative step before moving on to QIP experiments.

3.3.2 Magnetic field alignment

In our setup, the static magnetic field is applied through a bar magnet situated on top of the sample. The orientation of the magnet is controlled through two rotation stages (Figure 3.3).

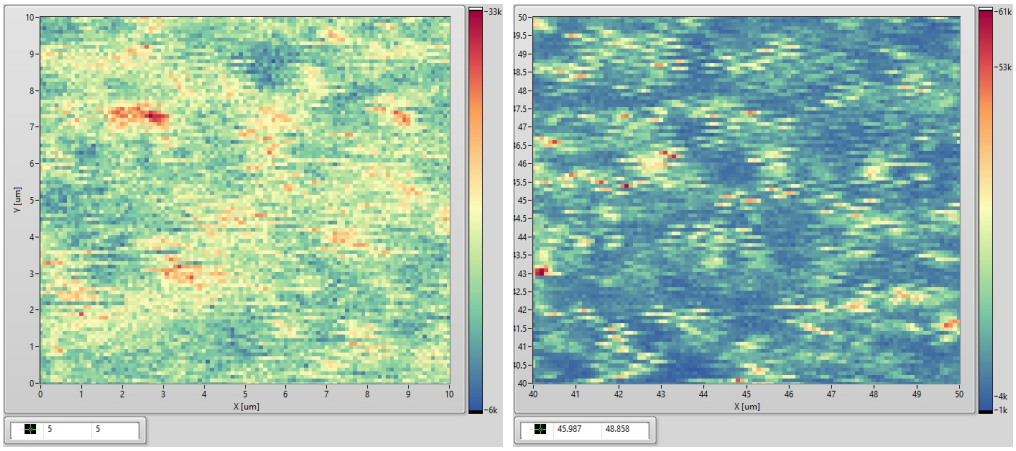

Figure 3.2: The photoluminescence scans before and after the optical alignment of the setup [15].

Using these stages, we had to determine the change in the applied magnetic field strength on a particular center with the two rotation angles of the two rotation stages, R1 and R2 respectively.

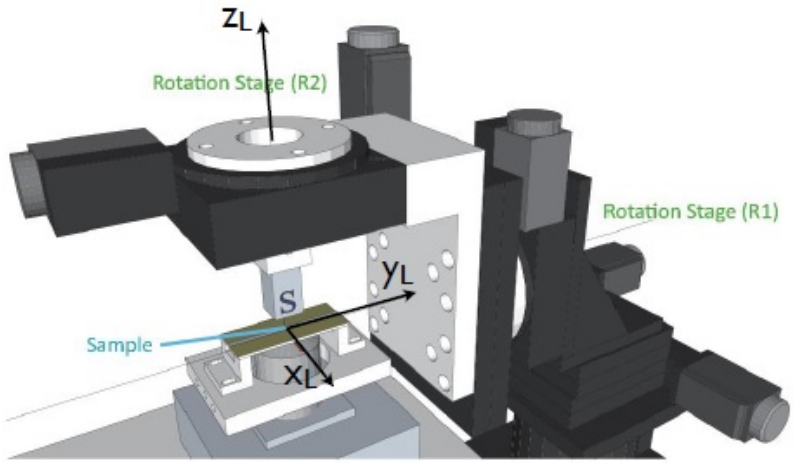

Figure 3.3: The rotation stages used to control the alignment of the magnet [7].

The z component of the magnetic field strength is determined by measuring the difference between the transition frequencies corresponding to the $(m_s = 0 \leftrightarrow m_s = +1)$ and the $(m_s = 0 \leftrightarrow m_s = -1)$ transitions in the ODMR spectrum (Figure 3.4) [15], since the difference between these two transitions is equal to $2\gamma_e B_z$, and γ_e (gyromagnetic ratio of the electron spin) is known.

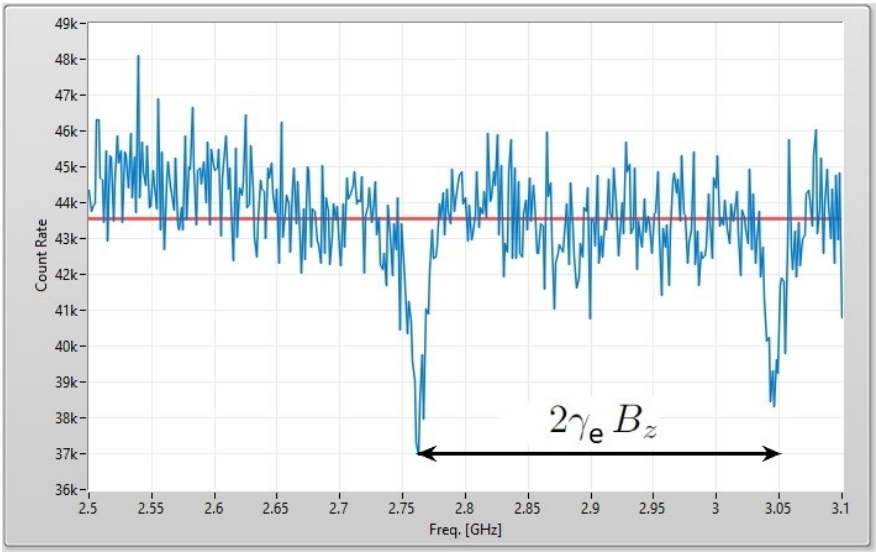

Figure 3.4: A typical ODMR spectrum, used to determine the two ESR transition frequencies [15].

The relation of the strength of the magnetic field v/s the angle R2 is supposed to fit a cosine curve [14]. Figure 3.5 shows a plot of the difference in the ODMR peak frequencies v/s the angle R2 (in degrees), for a fixed value of R1 = 84 degrees. We fitted the plot to the model $y = a|\cos(bx + c)|$, where y is the difference in the ODMR peak frequencies, x is the angle R2(in degrees), and a, b and c are the fitting parameters. We get a great fit for the results as shown (with an R^2 value of 0.99) in Figure 3.5. The z component of the magnetic field strength also follows the same relation, as it is linearly proportional to the difference in the ODMR peak frequencies.

Using these results, we were able to determine the orientation needed to apply the maximum magnetic field strength on our specific center, and we later proceeded to MW experiments using this specific orientation of the magnetic field.

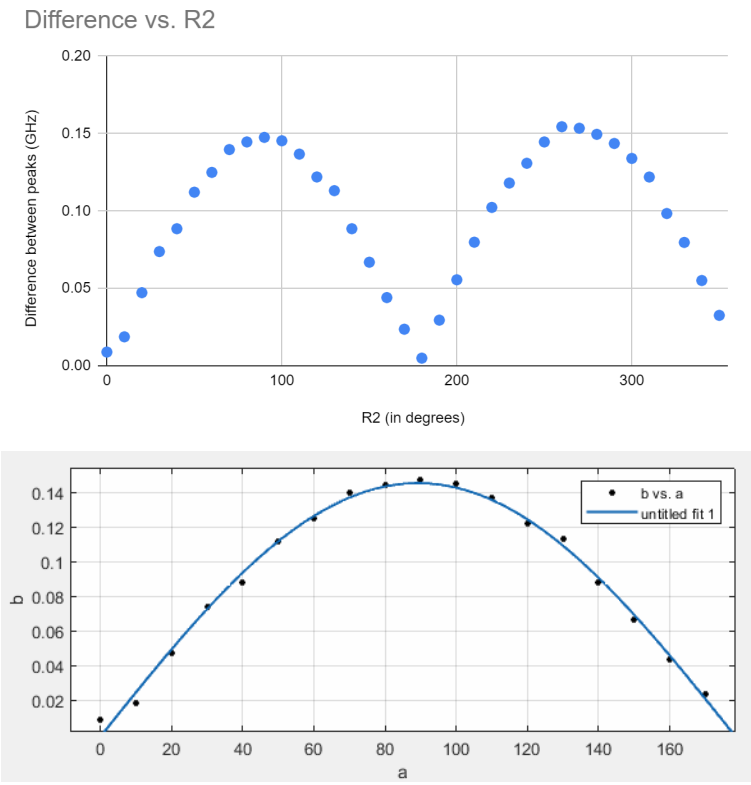

Figure 3.5: The results for the variation of magnetic field strength with angle R2; fit of the data with a sinusoidal curve [15].

3.3.3 Power Level Measurements

During initial ODMR experiments, the second transition peak's amplitude was significantly shorter than the first transition peak (Figure 3.6). One of the possible reasons for this was attributed to power loss in the cables of the ODMR MW circuit at higher frequencies. To confirm this, we performed power level measurements after each component of the circuit. This also helped me understand the use of the pulsed MW circuit components, both while performing ODMR experiments, as well as QIP experiments using the AWG (Arbitrary Waveform Generator). A schematic of the pulsed MW circuit is shown in Figure 3.7.

First, the Apsin generates an MW wave of the required frequency. The wave then goes to the RF IN input of a switch, which chooses between the output RF OUT1 or RF OUT2 depending on whether the AWG is being used or not being used respectively. In case of ODMR experiments, the wave directly goes to the RF OUT2 terminal of the second switch.

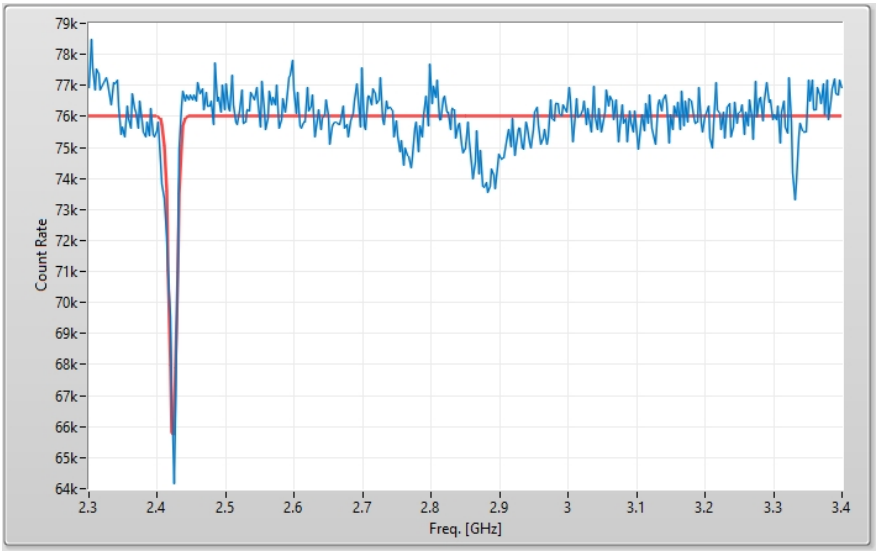

Figure 3.6: The ODMR spectrum with a much smaller amplitude of the second transition peak [15].

In case of AWG experiments, the AWG generates a RF pulse (usually of around 400 MHz frequency) which goes to the frequency mixer, where it is mixed with the wave generated by the Apsin. On mixing the two waves of different frequencies, waves of two frequencies (one with the sum and one with the difference of the frequencies of the Apsin and the AWG) are formed, which pass through a pre-amplifier, where the signal is amplified by 15 dB. The signal then goes to the RF OUT 1 terminal of the second switch. From here, the path of the signal is the same for both ODMR and AWG experiments. The pulse first passed through a 39 dB amplifier, after which it goes through a high pass filter (1700-3800 MHz). The high pass filter ensures that the lower frequency component of the wave generated in the frequency mixer in AWG experiments is discarded. The pulse then passes to a circulator (to suppress reflections from the sample) before finally moving on to the sample.

Since we wanted to check the ODMR MW circuit, we measured the power levels at the points labelled 1-5 in Figure 3.7, which helped us determine that there was indeed a significant power loss in some of the cables at higher frequencies. The power level readings shown in Figure 3.7 are at the frequency 3.1 GHz (high frequency). We later replaced these cables in the circuit to obtain much better ODMR spectras.

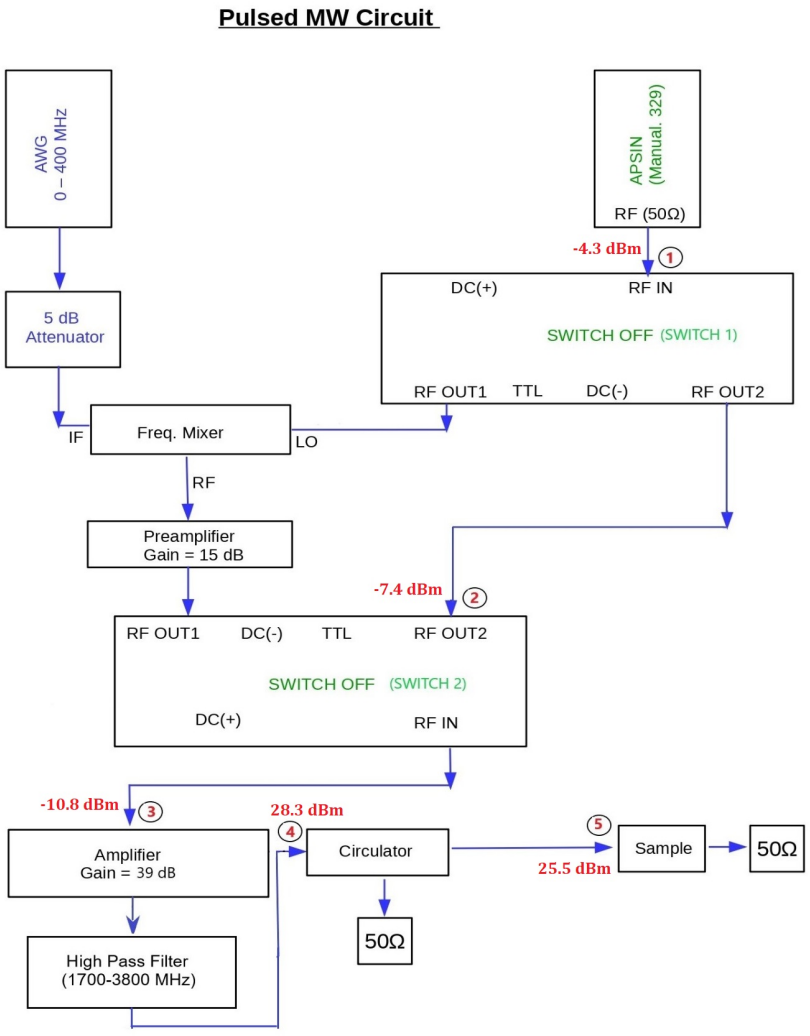

Figure 3.7: A schematic of the pulsed MW circuit, with power levels measured at points 1-5 [15].

Chapter 4

Electron Spin Control

Optimal control forms an important area of research in Quantum Information Processing (QIP). In this chapter, I talk about the theory and experimental implementation of some electron spin control techniques, as well as their uses in QIP.

4.1 Rabi oscillations

4.1.1 Theory

As mentioned in Chapter 1, the electron spin in an NV^- center is a spin $S = 1$ particle, which means that it has three states $m_s = 0$, +1 and -1. In optical experiments, after determining the two transition frequencies ($m_s = 0 \leftrightarrow m_s = +1$ and $m_s = 0 \leftrightarrow m_s =$ -1) in the ODMR spectrum, we choose the control MW field to be resonant with one of these transitions, thus restricting ourselves to the $m_s = 0 \leftrightarrow m_s = +1$ or the $m_s = 0 \leftrightarrow m_s =$ -1 subspace. In such a subspace in the NV center, the $m_s = 0$ state (called the ground state) scatters photons at a higher rate than the $m_s = \pm 1$ state (called the excited state).

In optical experiments, we first apply an 'initialization' laser pulse, which, when applied for a sufficiently long duration, initializes the electron spin completely in the ground state. Next, we apply a MW pulse (generated by a combination of the Apsin and the AWG) with a carrier frequency equal to the transition frequency of the subspace we've chosen, for

a variable time τ. This MW pulse drives the transition between the ground and excited states. Finally, we apply a 'readout' laser pulse, which measures the photoluminescence, by measuring the number of photons scattered by the state. The count rate is determined by dividing the total number of photons by the readout laser pulse duration.

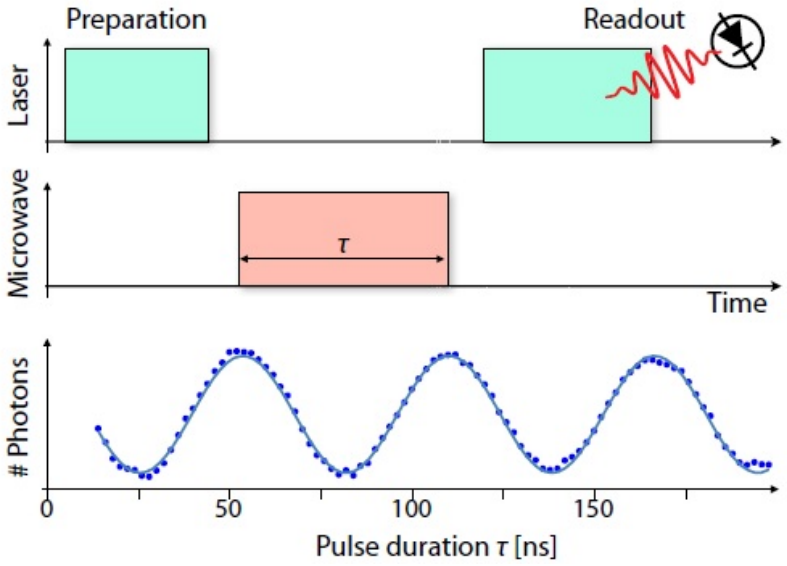

Figure 4.1: The pulse sequence for measuring Rabi oscillations, and the observed signal [1].

The system starts out in the ground state, after the initialization pulse, therefore having the maximum count rate. On applying the MW pulse, the state slowly starts transitioning to the excited state, resulting in a decrease in the count rate. When the rate reaches a minimum, the state has transitioned completely to the excited state. On applying the MW pulse for longer, the state starts transitioning back to the ground state. Therefore, when the count rate or photoluminescence (number of photons) is plotted against the variable MW pulse duration τ, we see oscillations, which are called Rabi oscilations. The frequency of these oscillations (called the Rabi frequency) is equal to the product of the gyromagnetic ratio of the electron (γ_e) and the strength of the control magnetic field (B_1). The pulse sequence and observed signal are shown in Figure 4.1.

4.1.2 Calculation of the state evolution and simulations

After the first initialization laser pulse, the system is completely in the ground state. We call this state s_0, where

$$s_0 = \begin{bmatrix} 1 \\ 0 \end{bmatrix}.$$

The total rotating frame Hamiltonian that the state evolves under the effect of during the application of the MW pulse is:

$$H_{rot} = (\nu_0 - \nu_{mw})S_z - \nu_1[\cos\phi S_x - \sin\phi S_y]$$

Here, since the carrier frequency of the MW pulse ν_{mw} is set to be equal to the transition frequency ($\nu_{mw} = \nu_0$), the resulting Hamiltonian is:

$H_{rot} = -\nu_1[\cos\phi S_x - \sin\phi S_y]$, i.e only the control Hamiltonian.

The state evolves under the unitary $U_0 = \exp(-iH_{rot}t) = \exp\left(i\nu_1 t[\cos\phi S_x - \sin\phi S_y]\right)$, where t is the duration for which the MW pulse is applied (in our case τ). For simplicity's sake, we choose $\phi = 0$. Calculations with a different ϕ don't affect the resulting ground state population (which we measure).

$$\implies U_0 = \exp(i\nu_1\tau S_x) = \cos(\tfrac{\nu_1\tau}{2})I + 2i\sin(\tfrac{\nu_1\tau}{2})S_x = \begin{bmatrix} \cos(\frac{\nu_1\tau}{2}) & i\sin(\frac{\nu_1\tau}{2}) \\ i\sin(\frac{\nu_1\tau}{2}) & \cos(\frac{\nu_1\tau}{2}) \end{bmatrix}$$

The resultant state s_1 is:

$$s_1 = U_0 s_0 = \begin{bmatrix} \cos(\frac{\nu_1\tau}{2}) & i\sin(\frac{\nu_1\tau}{2}) \\ i\sin(\frac{\nu_1\tau}{2}) & \cos(\frac{i\nu_1\tau}{2}) \end{bmatrix} \begin{bmatrix} 1 \\ 0 \end{bmatrix} = \begin{bmatrix} \cos(\frac{\nu_1\tau}{2}) \\ i\sin(\frac{\nu_1\tau}{2}) \end{bmatrix}$$

The density matrix of the resultant state s_1 is:

$$\rho_1 = s_1 s_1^T = \begin{bmatrix} \cos(\frac{\nu_1\tau}{2}) \\ i\sin(\frac{\nu_1\tau}{2}) \end{bmatrix} \begin{bmatrix} \cos(\frac{\nu_1\tau}{2}) & -i\sin(\frac{\nu_1\tau}{2}) \end{bmatrix}$$

$$\implies \rho_1 = \begin{bmatrix} \cos^2(\frac{\nu_1\tau}{2}) & -i\sin(\frac{\nu_1\tau}{2})\cos(\frac{\nu_1\tau}{2}) \\ i\sin(\frac{\nu_1\tau}{2})\cos(\frac{\nu_1\tau}{2}) & \sin^2(\frac{\nu_1\tau}{2}) \end{bmatrix}$$

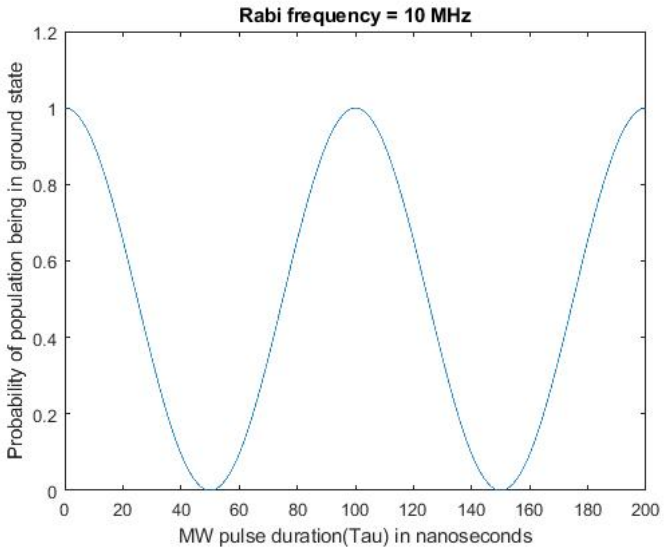

Figure 4.2: Rabi oscillations, with a Rabi frequency of 10 MHz [15].

The diagonal elements (1,1) and (2,2) of the density matrix give the populations of the ground state and excited state respectively. We measure the population of the ground state, and as expected, the ground state population evolves with the pulse duration τ as $\cos^2(\pi\nu_1\tau)$.

During the initial period of my project, I had simulated the effect of the pulse sequence used to measure Rabi oscillations on a single qubit system. One of the results is shown in Figure 4.2. The Rabi frequency $\nu_1 = \gamma_e B_1$ can be varied by varying the control magnetic field strength B_1. The plot shown in Figure 4.2 is of Rabi oscillations with a Rabi frequency of 10 MHz and a magnetic field strength of 0.357 mT. The MW pulse duration τ is varied from 0 to 200 ns, in increments of 0.2 ns.

4.1.3 Experimental implementation

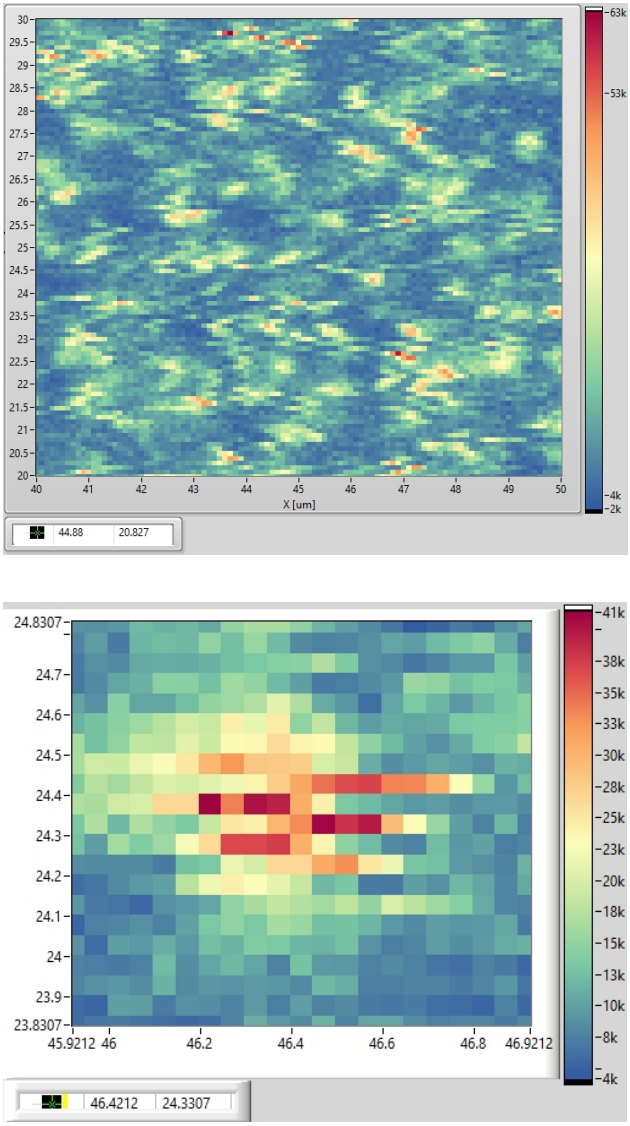

Figure 4.3: A coarse and fine scan of the diamond sample [15].

Before performing any spin control experiments, we first perform a 'z scan' where we fix the x-y plane and vary the z position. For different z positions, we measure the photon count rate from the NV center, to determine which z position gives us a high photon count rate from the NV center. Next, we perform a 'coarse' X-Y scan of the sample, to determine the exact locations of an NV center. Once we've found a center, we zoom in on it's location using a fine scan, so as to accurately pinpoint the position of the center. The images of a

coarse and fine scan in our NV setup are shown in Figure 4.3. The position of the center is then noted for future use.

Next, we perform an ODMR scan to determine the two transition frequencies of our centers, and set the control MW field frequency to be one of these frequencies (depending on which electron spin subspace we want to look at).

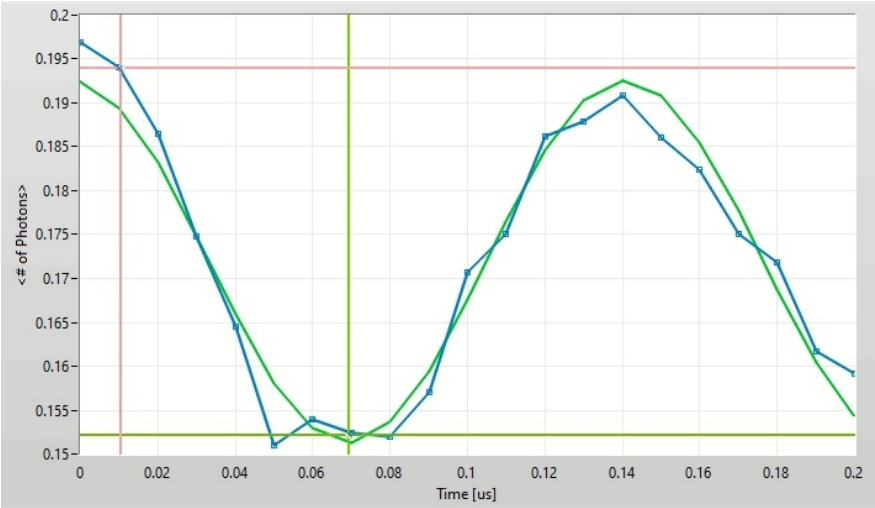

Figure 4.4: Rabi oscillations obtained along with a fit to the model, with a Rabi frequency = 6.98 MHz [15].

After that, we move on to our Rabi experiments. The control magnetic field strength can be varied by varying the amplitude, and the MW pulse duration can also be varied. Usually for hard Rabi experiments (Rabi frequency > 2 MHz), the maximum pulse duration does not exceed 400 ns, to prevent the burning of the wire. After the readout laser pulse (during which the photoluminescence is measured), we do not measure the photoluminescence for some time, but the laser is kept on during this time (idle time). During the idle time, the laser keeps pumping the population to the ground state. After the idle time, the photoluminescence is again measured for a longer duration than the readout laser pulse (in our case, five times as long as the readout laser pulse). The ratio of the two signals is taken, as it is less sensitive to fluctuations of the laser intensity or drifts of the position of the microscope [1]. A typical result of experimental Rabi oscillations is shown in Figure 4.4. The y axis in Figure 4.4 (labelled '<# of Photons>' is the ratio of the two photoluminescence counts. The data is then fitted to a $y = a + b\cos^2(cx + d)$ model (where y is the photoluminescence, x is the

variable time τ, a, b, c and d are the fitting parameters and $c = \frac{\nu_1}{2}$) and the Rabi frequency ν_1 is determined.

The most important use of measuring Rabi oscillations is to determine the π pulse duration, i.e the time taken for the state to go from the ground state to the excited state. The π and $\frac{\pi}{2}$ pulse durations are very important for many spin control experiments.

4.2 Free Induction Decay

4.2.1 Theory

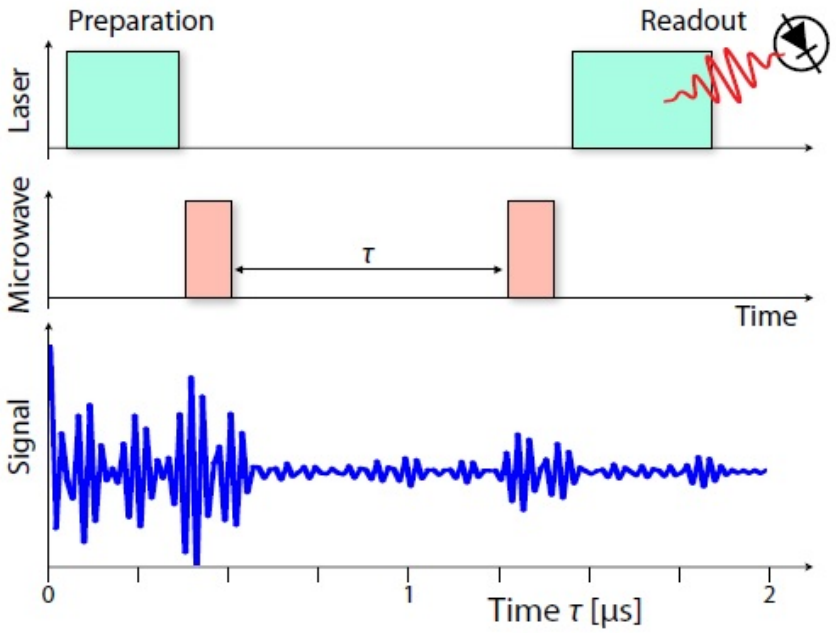

Figure 4.5: The pulse sequence for measuring FID, and the observed signal. The flip angles and phases of the two MW pulses are $\frac{\pi}{2}$ - x and $\frac{\pi}{2}$ - ϕ respectively [1].

A spin faces two types of decoherence or relaxation - longitudinal relaxation and transverse relaxation. The longitudinal relaxation time is characterized by T_1, while the transverse relaxation time is characterized by T_2. However, the actual transverse relaxation time of spins interacting with the environment (called T_2^*) is shorter than the ideal transverse relaxation time T_2. We can determine the unprotected relaxation time T_2^* of a spin by measuring the

free induction decay (FID) of the signal, and fitting the data to an exponential decay model. It also helps us determine the coupling of the electron spin to its neighbouring ^{14}N nuclear spin.

In FID experiments, first the system is initialised to the ground state using an initialization laser pulse, after which a $\frac{\pi}{2}$-x (rotation of the state by $\frac{\pi}{2}$ radians about the x axis) transfers the system to a superposition state $\frac{|0\rangle+i|1\rangle}{\sqrt{2}}$ (in the x-y plane), where $|0\rangle$ is the ground state, and $|1\rangle$ is the excited state. Next, we allow the system to freely evolve for a variable time τ. During this time, the electron spin freely precesses in the x-y plane. Ideally, the precession frequency of the spin should be equal to the control magnetic field's frequency (i.e the spin precession frequency should remain unchanged from before), but due to the random interaction of the spin with its environment (such as the coupling of the spin to multiple ^{13}C nuclear spins), there is an offset of the spin frequency with the control magnetic field's frequency. Finally, the system is converted back to the populations of the ground and excited state with a $\frac{\pi}{2}$-ϕ_d pulse, where $\phi_d = 2\pi\nu_d\tau$. Here ν_d is the detuning frequency. Finally, we plot the ground state population (or the photoluminescence) vs the variable free evolution time τ. The complete pulse sequence and observed signal of an FID measurement is shown in Figure 4.5.

4.2.2 Calculation of the state evolution and simulations

In this section, I will only be showing the state evolution calculation for a single spin system. Calculating a two spin system's (consisting of an electron and a ^{14}N nuclear spin) evolution has three major differences:

- The state is in a $2 \otimes 3 = 6$ dimensional subspace, and all calculations happen in this subspace.
- The free evolution Hamiltonian has an extra term - the secular hyperfine coupling term ($A_\parallel$).

For a single spin system, we first apply the initialization laser pulse, which initializes the system to the ground state. We call this state s_0, where

$$s_0 = \begin{bmatrix} 1 \\ 0 \end{bmatrix}.$$

The total rotating frame Hamiltonian that the state evolves under the effect of during the application of the $\frac{\pi}{2}$ MW pulse is:

$$H_{rot} = (\nu_0 - \nu_{mw})S_z - \nu_1[\cos\phi S_x - \sin\phi S_y].$$

Here, the carrier frequency of the MW pulse ν_{mw} is set to be equal to the transition frequency ($\nu_{mw} = \nu_0$). Also, as the rotation is about the x axis, $\phi = 0$. Therefore, the resulting Hamiltonian is:

$$H_{rot} = -\nu_1 S_x$$

The state evolves under the unitary $U_0 = \exp(-iH_{rot}t) = \exp(i\frac{\pi}{2}S_x)$, where t is the duration of the $\frac{\pi}{2}$ pulse.

$$\implies U_0 = \cos(\tfrac{\pi}{4})I + 2i\sin(\tfrac{\pi}{4})S_x = 1/\sqrt{2}\begin{bmatrix} 1 & i \\ i & 1 \end{bmatrix}.$$

The resultant state s_1 is:

$$s_1 = U_0 s_0 = \tfrac{1}{\sqrt{2}}\begin{bmatrix} 1 & i \\ i & 1 \end{bmatrix}\begin{bmatrix} 1 \\ 0 \end{bmatrix} = \tfrac{1}{\sqrt{2}}\begin{bmatrix} 1 \\ i \end{bmatrix}.$$

Next, the system is allowed to evolve for a variable free evolution time τ. Since I assume my control field frequency to be resonant with the transition frequency, my free evolution Hamiltonian is zero. To simulate a decay, I multiply an exponential decay term $\exp(-\frac{\tau}{T_2^*})$ (where T_2^* is the unprotected transverse relaxation time) to the off-diagonal elements of the state s_1. The simulated decay is not shown in the calculations, however, the results of such a simulated decay are shown later on in this section. The best way to simulate such a decay (without having to use a decay term) is to consider a system of multiple non-interacting spins, which all have a different off-resonant static Hamiltonian terms, and allow such a system to evolve freely for a variable time τ. I have simulated the results for such a system in Section 4.3.1.

The state s_1 then evolves under the effect of the $\frac{\pi}{2}$-ϕ_d MW pulse, with the Hamiltonian:

$$H_1 = -\nu_1[\cos(\phi_d)S_x - \sin(\phi_d)S_y],$$

where $\phi_d = 2\pi\nu_d\tau$. Here ν_d is the detuning frequency. The unitary corresponding to this Hamiltonian is $U_1 = \exp(-iH_1t)$ (here t is the duration of the $\frac{\pi}{2}$ pulse)

$$= \exp(i\nu_1 t(\cos(\phi_d)S_x - \sin(\phi_d)S_y)) = \exp(i\tfrac{\pi}{2}(\cos(\phi_d)S_x - \sin(\phi_d)S_y)).$$

On simplifying this, we get:

$$U_2 = \tfrac{1}{\sqrt{2}}\begin{bmatrix} 1 & i\cos(\phi_d) - \sin(\phi_d) \\ i\cos(\phi_d) + \sin(\phi_d) & 1 \end{bmatrix}.$$

The final state s_2 is:

$$s_2 = U_2 s_1 = \tfrac{1}{2}\begin{bmatrix} 1 & i\cos(\phi_d) - \sin(\phi_d) \\ i\cos(\phi_d) + \sin(\phi_d) & 1 \end{bmatrix}\begin{bmatrix} 1 \\ i \end{bmatrix}$$

$$\implies s_2 = \tfrac{1}{2}\begin{bmatrix} 1 - \cos(\phi_d) - i\sin(\phi_d) \\ i\cos(\phi_d) + \sin(\phi_d) + i \end{bmatrix}.$$

The density matrix corresponding to the state s_2 is: $\rho_2 = s_2 * s_2^T$. To measure the final signal, we measure the (1,1) element of ρ_2, which gives us the population in the ground state, and is:

$$\rho_2(1,1) = \tfrac{1}{2}[1 - \cos(\phi_d)].$$

I have simulated the effects of the FID pulse sequence (with and without the simulated decay) on both a single spin as well as a two spin system (electron and ^{14}N nuclear spin). The results for a single spin system are shown in Figure 4.6, while the results for a two spin system are shown in Figure 4.7. The detuning frequency in both cases is 20 MHz, the Rabi frequency is 10 MHz (hard Rabi pulse so as to excite all three transitions corresponding to the nuclear spin: $m_n = 0$, +1 and -1), the secular hyperfine coupling $A_\parallel = 2.16$ MHz, and the free evolution time is varied from 0 to 200 ns in increments of 0.2 ns for the single spin system, and from 0 to 2000 ns in increments of 2 ns for the two spin system. The T_2^* for the simulated decay of the single spin system is 100 ns, and for the two spin system is 1000 ns.

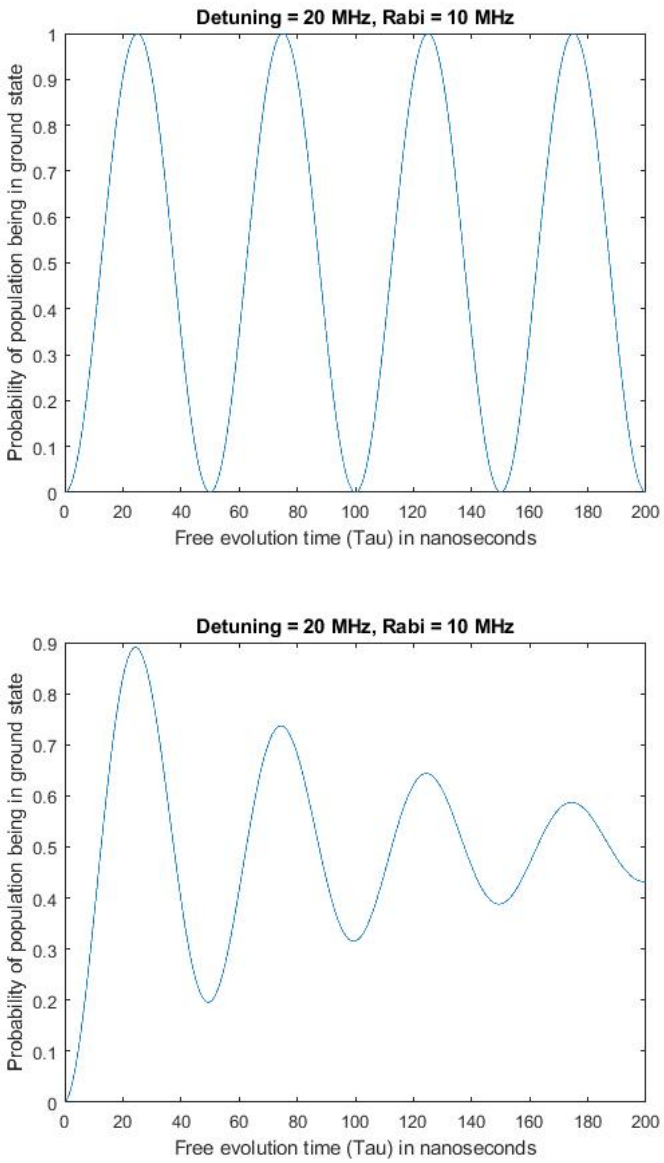

Figure 4.6: The FID signal for a single spin system, with and without decay [15].

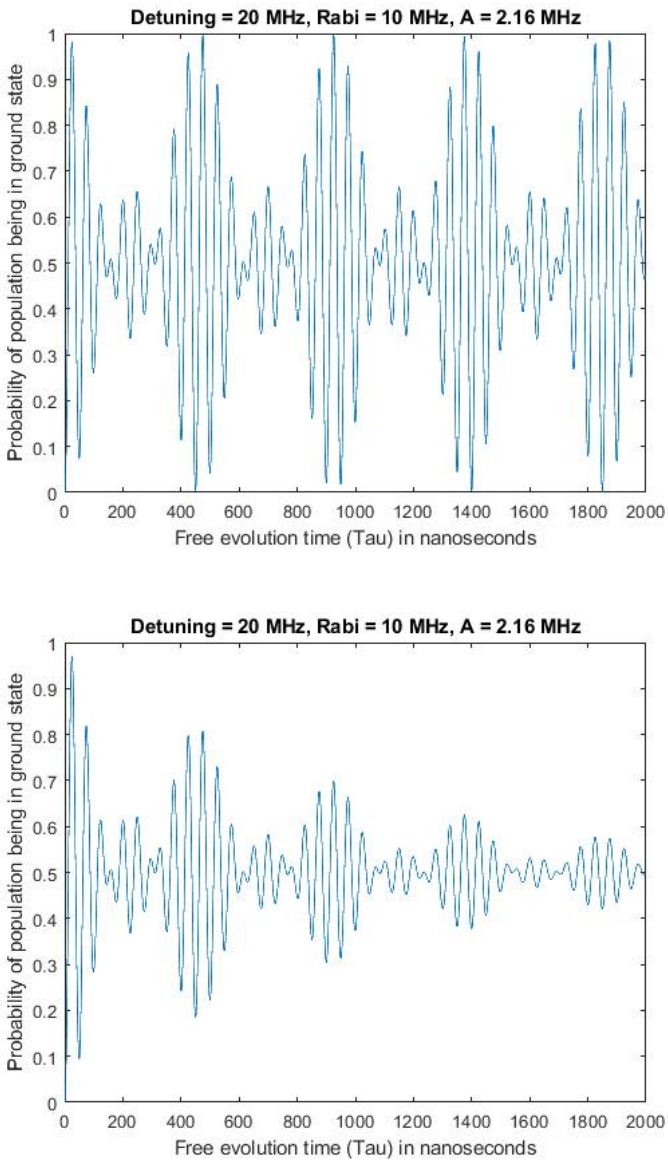

Figure 4.7: The FID signal for a two spin system (electron spin coupled to a ^{14}N nuclear spin), with and without decay [15].

The fast fourier transform (FFT) of the FID signal from the time domain to the frequency domain can give us a lot of useful data as well. The results of the FFT spectrum of the FID signal of a single spin system with decay is shown in Figure 4.8. As expected, there is a single peak at the detuning frequency $\nu_d = 20$ MHz. In the case of a simulated decay, we obtain a Lorentzian peak. The inverse of the half-maximum width of the Lorentzian peak gives us the T_2^* of the system.

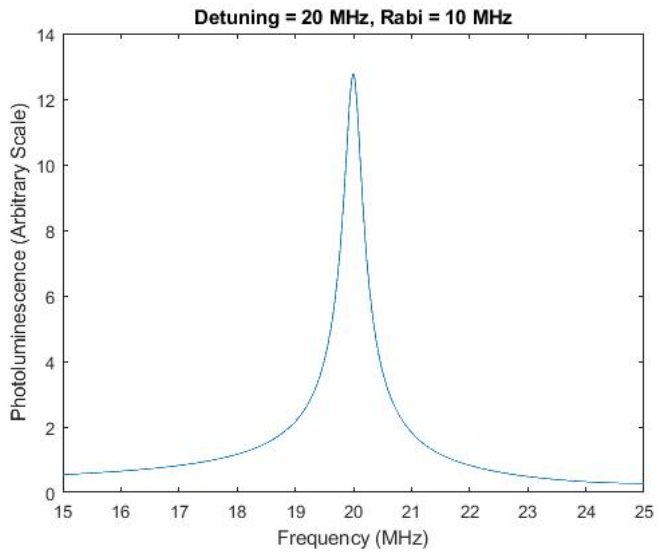

Figure 4.8: The FFT of the FID signal for a single spin system, with simulated decay [15].

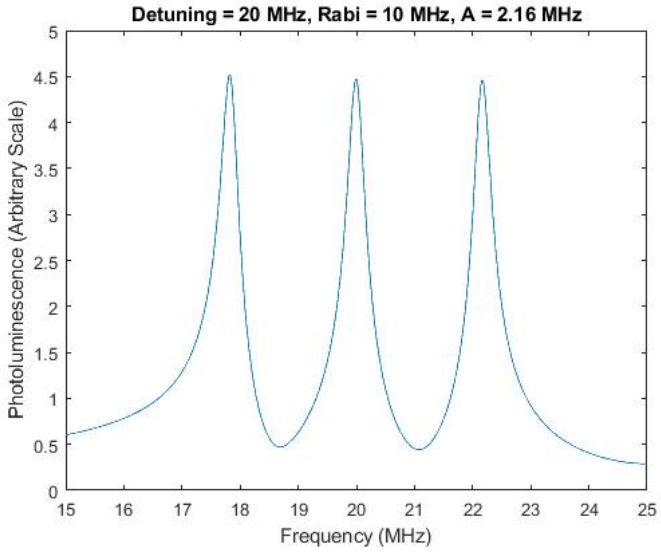

Figure 4.9: The FFT of the FID signal for a two spin system (electron spin coupled to a ^{14}N nuclear spin), with simulated decay [15].

The results of the FFT spectrum of the FID signal of a two spin system is shown in Figure 4.9. As expected, there are three peaks (corresponding to the transitions of ($m_s = 0 \leftrightarrow \pm 1$) for $m_n = +1$, 0 and -1 respectively. In the case of a simulated decay, we obtain

Lorentzian peaks. The inverse of the width at half-maximum of the Lorentzian peaks gives us the T_2^* of the system.

4.2.3 Experimental Implementation

To perform FID measurements, we first choose a center, take an ODMR scan, and choose a particular electron transition frequency, and measure the Rabi oscillation according to the procedure mentioned in Section 4.1.3.

After performing Rabi measurements, we note down the MW $\frac{\pi}{2}$ pulse duration. In the 'FID experiment' section, we use this $\frac{\pi}{2}$ pulse duration for both the MW pulses used in the experiment. The total free evolution time τ and the time increments can be varied. The detuning frequency ν_d can also be varied, and is usually set to 20 MHz. A typical experimental FID signal is shown in Figure 4.10.

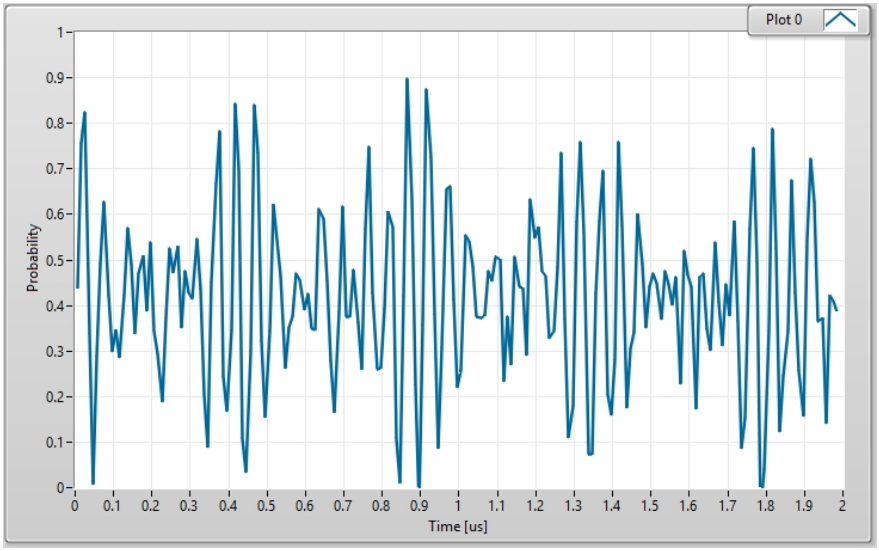

Figure 4.10: A typical experimental FID signal. The y axis is the probability of the population being in the ground state [15].

Next, we measure the FFT spectrum of the FID signal, after some additional 'data processing' of the FID signal data. In the data processing, we first perform 'baseline correction', where we adjust the baseline so that the data is centered around y = 0. Next, we apply a Gaussian window to the signal, in order to minimize the noise that arises at higher values

of τ. Finally, we apply a 'zero filling' of 8192 points, wherein we add zeros at the end of the FID signal till there are a total of 8192 points in the signal. This is done because the FFT algorithm always used the same number of points in the FID signal data to obtain the FFT spectrum, and also because more data points are useful in getting more clear peaks. The FFT spectrum (obtained after data processing) of an experimental FID signal is shown in Figure 4.11. The FFT has two very important uses in our experiments. We determine the T_2^* of the spin using the method mentioned in Section 4.2.2. We also measure the offset of the central peak (corresponding to $m_n = 0$) from the detuning frequency, which tells us the offset of the control magnetic field frequency from the required transition frequency (an offset of the order of MHz is not visible in the ODMR scan), and thus helps us make the control magnetic field frequency perfectly resonant with the transition frequency.

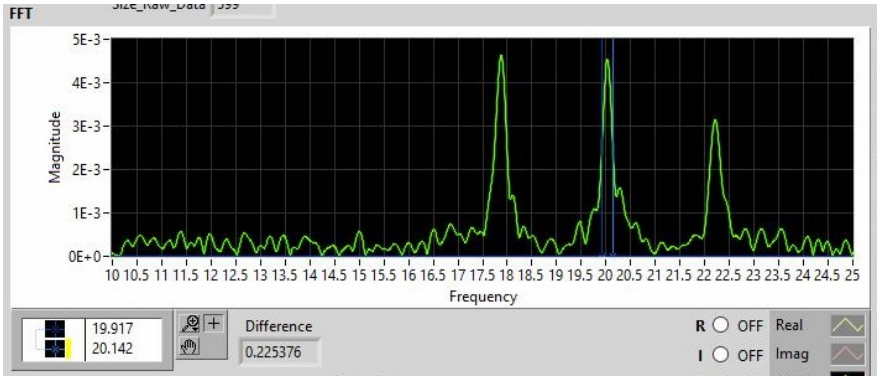

Figure 4.11: FFT spectrum of the experimental FID signal [15].

4.3 Dynamical Decoupling

4.3.1 Theory

One of the major challenges in QIP research using NV centers is the decoherence of the electron spin. The electron spin faces decoherence due to its random interaction with the system. The random interactions could be due to the fluctuating B field, or couplings to multiple nuclear spins (in the natural abundance sample that we use in our NV setup, the source is mainly due to the interaction of the electron spin with multiple ^{13}C spins). This reduces the transverse relaxation time of an unprotected spin from T_2 to T_2^* ($T_2 >$

T_2^*). Protecting the spin from interactions with the environment form an important area of current research. This is achieved by applying 'Dynamical Decoupling' (DD) pulse sequences which, as the name suggests, decouple the spin from the environment and thus increase the decoherence time of the electron spin.

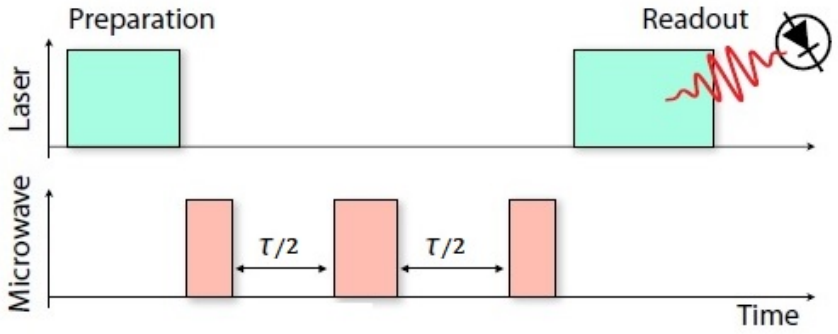

Figure 4.12: Pulse sequence for measuring a Hahn echo signal. The flip angles and phases of the MW pulses are $\frac{\pi}{2}$ - x, π - x and $\frac{\pi}{2}$ - x respectively [1].

The simplest DD pulse sequence is a Hahn-echo pulse sequence [8]. Here, the system is first initialised to the ground state by an initialization laser pulse. Next, a $\frac{\pi}{2}$ - x pulse brings the system to the superposition state $\frac{|0\rangle+i|1\rangle}{\sqrt{2}}$, i.e the +y axis. Then, we allow the system to freely evolve for a variable time duration $\frac{\tau}{2}$. During this time the electron spin starts precessing in the x-y plane, with a frequency that is offset from the frequency of the control magnetic field depending on the interaction of the spin with its environment. This leads to the T_2^* dephasing of the electron spin. Next, we apply a 'refocusing' π - x pulse. the refocusing pulse rotates/flips the spin about the x axis. If the spin is at an angle θ from the +y axis in the x-y plane after the free precession, it makes an angle $(\pi - \theta)$ with the +y axis after the refocusing pulse. Next, we allow the system to freely precess for $\frac{\tau}{2}$. This ensures that no matter the offset of the spin frequency from the frequency of the control magnetic field, the spin reaches the -y axis at the end of the second free precession. Finally, a $\frac{\pi}{2}$ - x pulse converts one of the coherences of the system (the y component of the spin) into the population difference between the $m_s = 0$ and $m_s = -1$ states, where it is measured using a readout laser pulse. The complete pulse sequence is shown in Figure 4.12.

The best way to simulate these results is to consider a system of N non-interacting electron spins, with different precession frequencies. The results of the simulation of such a system with $N = 100$ spins and $N = 500$ spins is shown in Figure 4.13. The blue signal corresponds to the dephasing or the decay of the signal, while the red signal corresponds to

its refocusing. The parameters used for the simulations in Figure 4.13 are the number of spins (N = 100 and 500 for the two simulations), the Rabi frequency (= 10 MHz for both simulations) and the offset of each spin's frequency from the frequency of the control magnetic field (the offset of each spin was set to be a random number from a uniform distribution between -0.5 MHz to 0.5 MHz).

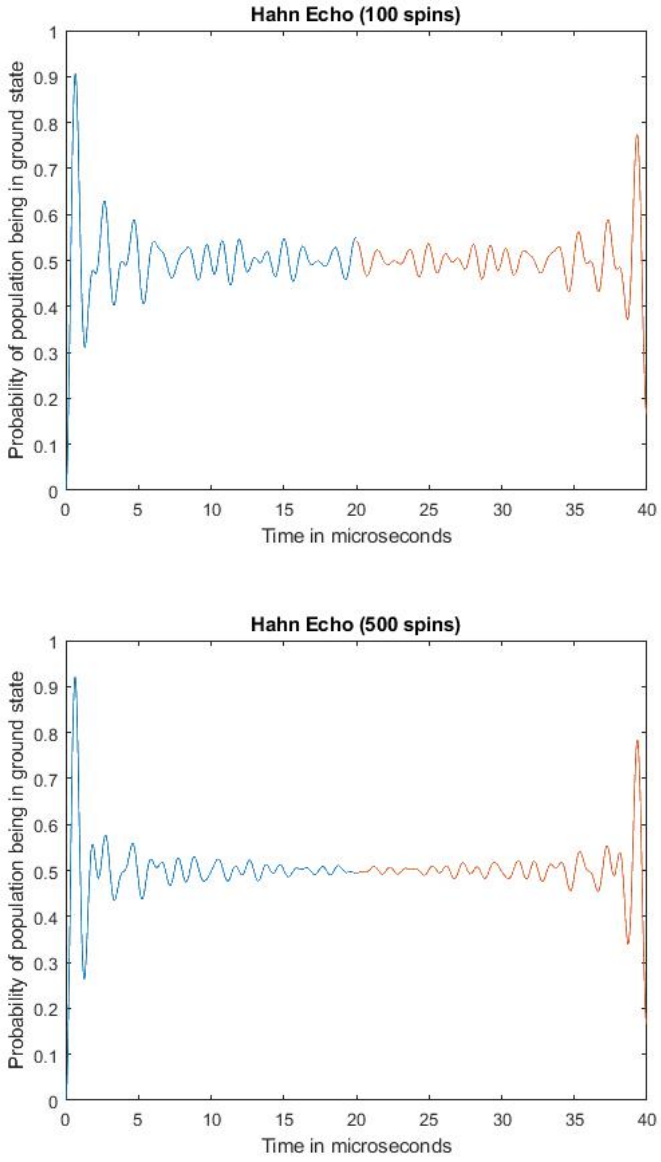

Figure 4.13: The dephasing and refocusing of a signal in a Hahn echo pulse sequence for a system of 100 and 500 spins [15].

When we increase the number of refocusing π - x pulses from 1 to N, we get a CPMG-N pulse sequence. Ideally, increasing the number of refocusing pulses should increase the T_2 time of the spin. However, a certain optimum is reached in experiments, owing to errors in applying the refocusing pulse.

4.3.2 Experimental Implementation

To perform Hahn echo and CPMG experiments, we first choose a center, perform an ODMR scan, choose a transition frequency, and measure the Rabi oscillations to determine the MW π and $\frac{\pi}{2}$ pulse durations. Using these times in the Hahn-echo segment of the experiments, we vary the total variable time duration τ and measure the signal decay (due to the protected transverse relaxation time T_2). Figure 4.14 shows the result of the Hahn echo signal.

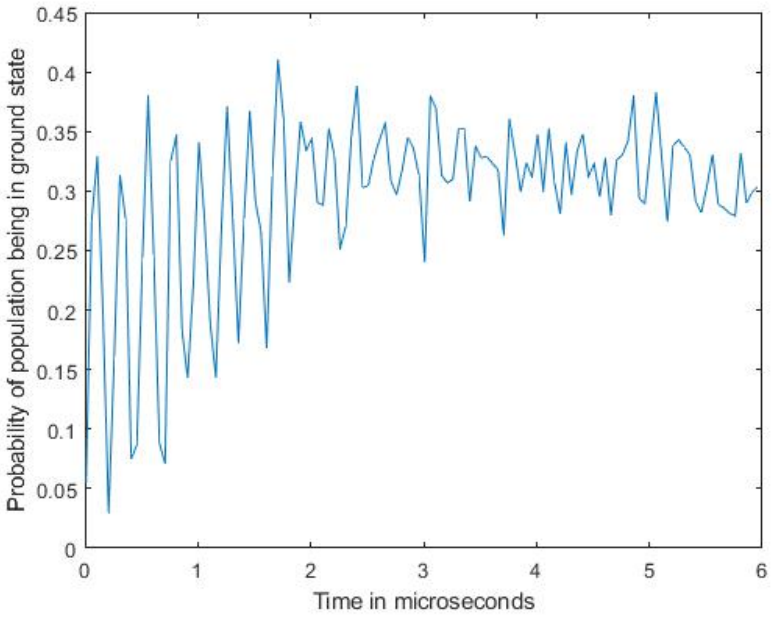

Figure 4.14: The Hahn echo signal [15].

The initial oscillations are suspected to be due to the coupling of the electron spin to the ^{14}N nuclear spin. Since the system decays from the excited state to a mixed state and because the photoluminescence of the excited state is lower than the ground state, we get a signal of the form $y = 1 - \exp(-\frac{\tau}{b})$, where y is the probability of the population being in

the ground state.

To convert this into an exponential decay, I plot (1-y) vs τ. The plot of (1-y) vs τ is shown in Figure 4.15. Finally, we fit the data to the curve:

$$y = c + (a\exp(-\tfrac{\tau}{b})^n)\cos(d\tau)$$

where a, b, c, d and n are variable parameters, and b is the measured T_2 of the system. One of the fits of the Hahn echo signal is shown in Figure 4.16.

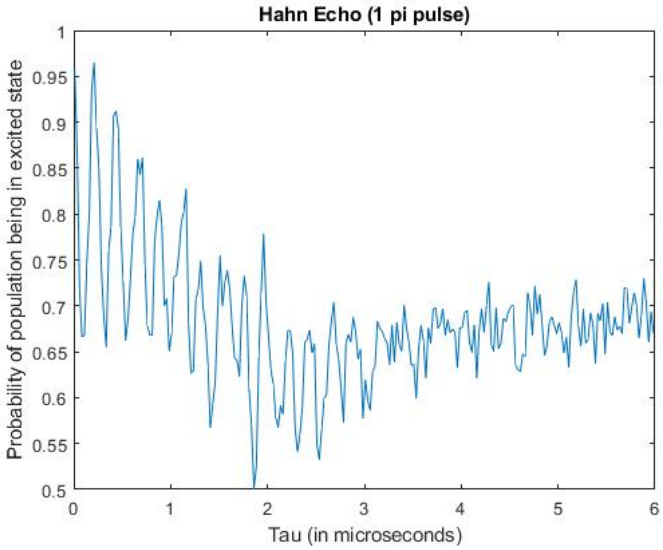

Figure 4.15: The Hahn echo signal decay [15].

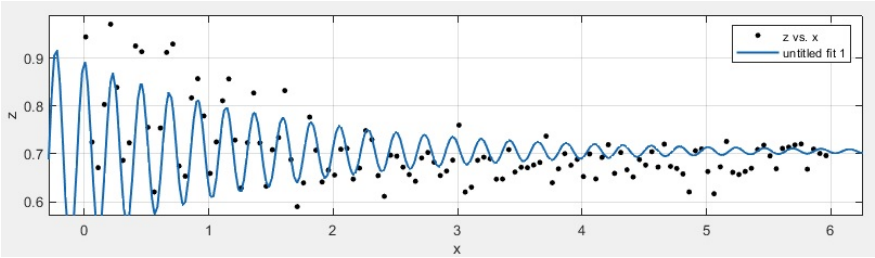

Figure 4.16: A fit of the Hahn echo signal decay curve with the theoretical model [15].

4.3.3 Results

We obtain the unprotected time of the electron spin T_2^* using the method detailed in section 4.2.2, and the protected time T_2 of the spin after applying the Hahn echo and CPMG pulse sequences by measuring the value of 'b' for the best fit of the signal to the above mentioned theoretical model. In our experiments, we determined that the unprotected time $T_2^* = 1.89\mu$s, T_2 after Hahn echo = 3.02 μs, T_2 after CPMG - 2 = 6.68 μs and T_2 after CPMG - 4 = 9.31 μs.

After a CPMG-8 pulse sequence, the T_2 was found to be 7.36 μs, i.e lesser than the T_2 after a CPMG-4 pulse sequence. This is due to some experimental errors while implementing the pulse sequence, which we are currently trying to improve. Therefore, the optimal pulse sequence for the best decoherence of our system (currently) was CPMG - 4.

4.4 Quantum State Tomography

4.4.1 Theory

The goal of quantum state tomography is to reconstruct the entire state (i.e the density matrix of the state) in order to obtain the full information of the system [9]. The diagonal elements of the density matrix of the single qubit state are obtained from the count rate/photoluminescence (which is the observable in our system). The off-diagonal elements are also converted to diagonal elements using some operations, and the diagonal elements which result from conversion of the off-diagonal elements from these operations are once again obtained through the count rate/photoluminescence.

For a single qubit (the electron spin in our system), the density matrix can be written as:

$$\rho = aI_2 + b\sigma_x + c\sigma_y + d\sigma_z \tag{4.1}$$

where I_2 is the 2 dimensional identity matrix, and σ_x, σ_y and σ_z are the Pauli matrices. For a normalised system:

$$a = \frac{p_0 + p_1}{2} = \frac{1}{2}, \tag{4.2}$$

where p_0 and p_1 are the the populations in the ground and excited state respectively. The aim is to find the coefficients a, b, c and d. Also:

$$d = \frac{p_0 - p_1}{2} \tag{4.3}$$

The electron spin is first polarised to the ground state, and then we use the fact that the ground state has a higher fluorescence than the excited state, to determine the population in the ground state as:

$$r = r_{min} + p_0(r_{max} - r_{min}) \tag{4.4}$$

As mentioned in section 4.1.1, the entire population in the ground state (corresponding to $p_0 = 1$) results in the highest count rate r_{max}, while the entire population in the excited state (corresponding to $p_1 = 1$) results in the lowest count rate r_{min}. Using these, we can determine that:

$$p_0 = \frac{(r - r_{min})}{(r_{max} - r_{min})}; \tag{4.5}$$

$$p_1 = \frac{(r_{max} - r)}{(r_{max} - r_{min})}. \tag{4.6}$$

To get the values of r_{max} and r_{min} and thus determine the value of the coefficient 'a' (should be close to 0.5), we first initialize the system to the ground state using the laser pulse. Then, we apply no MW pulse operation to get the value of r_{max}, and an X_{180} (or π - x) MW pulse operation to get the value of r_{min}.

To get the coefficients of the off-diagonal elements, the operations $X_{90} = \exp(-\frac{i\pi\sigma_x}{4})$ and $Y_{90} = \exp(-\frac{i\pi\sigma_y}{4})$ are applied to transform the density matrix as:

$$X_{90}\rho X_{90}^{\dagger} = aI_2 + bS_x - dS_y + cS_z; \tag{4.7}$$

$$Y_{90}\rho Y_{90}^{\dagger} = aI_2 + dS_x + cS_y - bS_z. \tag{4.8}$$

By using the count rates obtained after the operations X_{90}, Y_{90} and NOOP (no operation) as r_X, r_Y and r_N respectively, we get:

$$b = \frac{1}{2} - \frac{r_Y - r_{min}}{r_{max} - r_{min}}; \tag{4.9}$$

$$c = \frac{r_X - r_{min}}{r_{max} - r_{min}} - \frac{1}{2}; \tag{4.10}$$

$$d = \frac{r_N - r_{min}}{r_{max} - r_{min}} - \frac{1}{2}. \tag{4.11}$$

Thus, we get the coefficients and can reconstruct the entire density matrix.

4.4.2 Experimental Implementation and Results

We experimentally reconstructed the density matrices for the states $|0\rangle$, $|1\rangle$, $|+\rangle$ and $|-\rangle$, where $|0\rangle$ is the ground state, $|1\rangle$ is the excited state, $|+\rangle = \frac{|0\rangle+|1\rangle}{\sqrt{2}}$ and $|-\rangle = \frac{|0\rangle-i|1\rangle}{\sqrt{2}}$. To prepare the $|0\rangle$, $|1\rangle$, $|+\rangle$ and $|-\rangle$ states, we perform NOOP, X_{180}, Y_{90} and X_{90} MW pulse operations after the initialization laser pulse.

Next, we apply the 3 types of MW pulses (NOOP, Y_{90} and X_{90}) on each of these states to get the values of r_X, r_Y and r_N respectively, determine the coefficients b, c and d, and reconstruct the entire density matrices of these states. The results for the density matrix coefficients b, c and d for each of the 4 states is given in the table below. The values in parantheses are the expected values of the coefficients. The value of the coefficient 'a' (determined from the method mentioned in section 4.4.1) is found to be 0.501. The large deviations from the expected values of 'c' for $|+\rangle$ and 'b' for $|-\rangle$ are due to some experimental errors in the phases of the pulses applied, and we are working on rectifying these errors.

State	b	c	d
$\|0\rangle$	0.012 (0)	0.041 (0)	0.45 (0.5)
$\|1\rangle$	0.008 (0)	0.054 (0)	-0.501 (-0.5)
$\|+\rangle$	0.496 (0.5)	0.186 (0)	-0.026 (0)
$\|-\rangle$	0.326 (0)	-0.515 (-0.5)	-0.007 (0)

Chapter 5

Nuclear Spin Control

To eventually perform gate operations with two or more qubits in NV centers, it is imperative to be able to control the ^{14}N and surrounding ^{13}C nuclear spins. In this chapter, I discuss some of the sequences involving MW and RF pulses that are used to control the ^{14}N nuclear spin, and the challenges associated with these operations.

5.1 Rabi oscillations

5.1.1 Theory

To perform nuclear spin Rabi oscillations, we consider a two spin system, consisting of a spin $S = \frac{1}{2}$ electron spin (we restrict ourselves to this subspace by choosing a particular transition frequency in the ODMR scan) and a spin $S = 1$ ^{14}N nuclear spin. I will be writing the states of this system as $|m_s, m_n\rangle$. The electron spin states are labelled as $|0\rangle$ and $|1\rangle$, while the nuclear spin states are labelled as $|0\rangle$, $|1\rangle$ and $|-1\rangle$.

We first apply an initialization laser pulse, which polarizes the electron spin to the ground state, and fully depolarizes the nuclear spin. Therefore, there is an equal population in the states $|0, 0\rangle$, $|0, 1\rangle$ and $|0, -1\rangle$ respectively. Next, we apply a 'selective' π - x MW pulse, which completely transfers the population of the state $|0, 0\rangle$ to $|1, 0\rangle$, but leaves the other states unaffected. The experimental implementation of such a selective pulse is described in

section 5.1.2.

Next, we apply an RF pulse with a carrier frequency corresponding to the transition $|1,0\rangle \leftrightarrow |1,1\rangle$ or $|1,0\rangle \leftrightarrow |1,-1\rangle$ for a variable time τ, which drives the population transfer between these states. Then, another selective π - x MW pulse brings back the population in the $|1,0\rangle$ to the $|0,0\rangle$ state. Finally, we apply a readout pulse to measure the population of the electron ground state, which measures the sum of the populations in the $|0,0\rangle$, $|0,1\rangle$ and $|0,-1\rangle$ states. The ground state population is plotted against the variable time τ to obtain Rabi oscillations. The contrast of the nuclear Rabi oscillations is one-third that of the electron Rabi oscillations, as only the population in the $|0,0\rangle$ state undergoes transfer. The complete pulse sequence and the selective MW and RF transitions are shown in Figure 5.1.

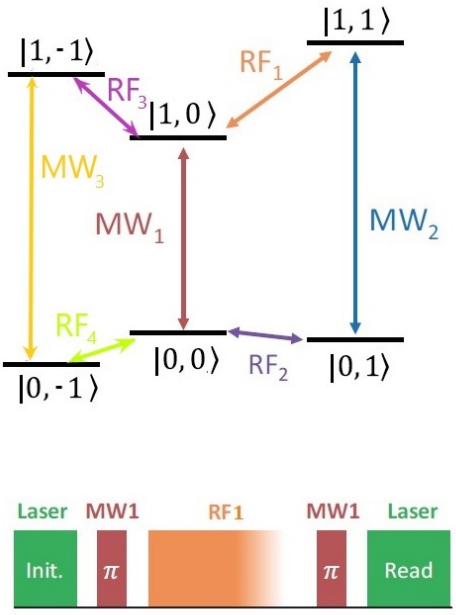

Figure 5.1: Energy levels and transitions of the two spin system, and the pulse sequence used to measure nuclear Rabi oscillations. The flip angles and phases of both MW_1 pulses are π - x. The RF_1 pulse is applied for a variable time τ [10].

5.1.2 Experimental implementation

To measure nuclear Rabi oscillations, we first choose an NV center, and choose a particular electron spin transition in the ODMR scan. Then we perform 'soft' electron Rabi oscillation experiments, i.e we measure Rabi oscillations with a low Rabi frequency of around 0.3 MHz (as compared to hard Rabi oscillations (used in Chapter 4) having a Rabi frequency of around 10 MHz). This helps us determine the Rabi frequency at which the MW pulse becomes selective, and excites only our desired state [11]. To confirm the selective transition, we note down the $\frac{\pi}{2}$ and π pulse durations of these transition selective MW pulses, and perform an FID experiment using the MW $\frac{\pi}{2}$ pulse duration. Taking the data-processed FFT of the signal should show us a single peak (corresponding to the transition of the state we choose), instead of three peaks corresponding to the transitions of all three nuclear spin states m_n = 0, +1 and -1. The data-processed FFT of a selective transition is shown in Figure 5.2. In Figure 5.2, only the transition corresponding to the nuclear spin state $m_n = 0$ is excited.

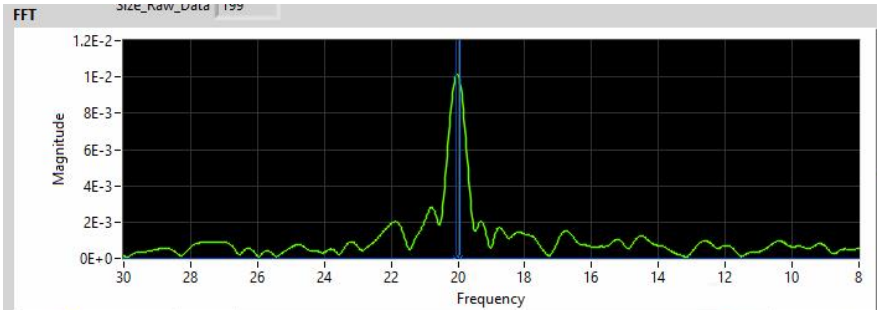

Figure 5.2: The data-processed FFT of an FID signal obtained by using selective transition MW pulses [15].

We apply a selective MW π - x pulse, after which we need to apply an RF pulse. The carrier frequency of the RF pulse is set to be equal to the transition that we want to drive (for example, $|1,0\rangle \leftrightarrow |1,1\rangle$), which is theoretically calculated using the Hamiltonian in Equation 2.6. As an example, in our experiment, the transition frequency of the $|1,0\rangle \leftrightarrow |1,1\rangle$ transition is theoretically determined to be 7.16 MHz (the static field strength B_{0z} is 16.09 mT). We sweep the RF frequency around this value, and measure the Rabi oscillations. The Rabi oscillations which have a good fit to the theoretical model $y = a + b\cos^2(cx + d)$ (where y is the photoluminescence, x is the time for which the RF pulse is applied, and a, b, c and d are the fitting parameters) will help us determine the actual frequency of the

particular transition in our experiment. The nuclear Rabi oscillations we observed for the transition corresponding to $|1,0\rangle \leftrightarrow |1,1\rangle$ (experimental RF frequency = 7.17 MHz) is shown in Figure 5.3. The y axis in Figure 5.3 (labelled 'Photoluminescence') is the same ratio of the photoluminescences as the one mentioned for electron spin Rabi experiments in section 4.1.2, and the x axis is the time in μs.

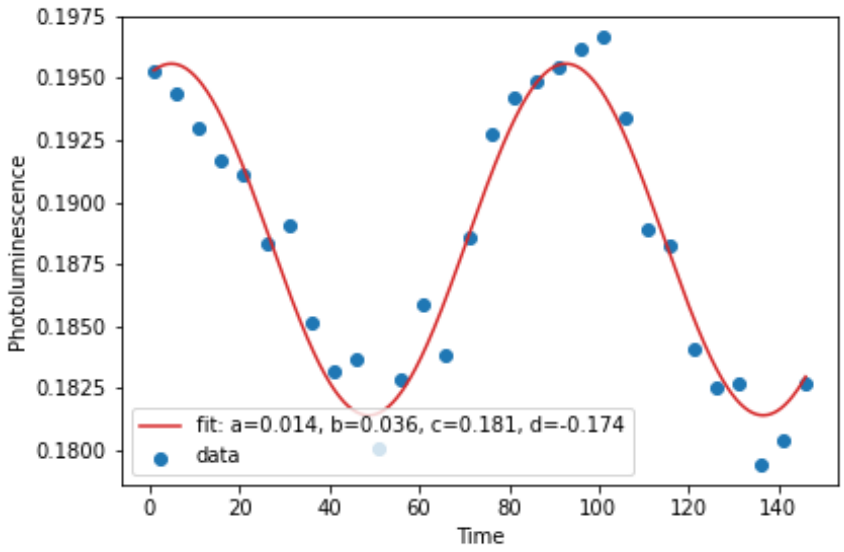

Figure 5.3: Nuclear Rabi oscillations observed for the transition $|1,0\rangle \leftrightarrow |1,1\rangle$ [15].

The Rabi oscillations are fit to a $y = a + b\cos^2(cx + d)$ model, and the nuclear Rabi frequency $\nu_{RF} = \frac{b}{2\pi}$ is determined. The Rabi frequency for the oscillations in Figure 5.3 is $\approx$ 11 kHz.

5.2 Free Induction Decay

5.2.1 Theory

To obtain a nuclear spin FID signal, we first apply an initialization laser pulse, which completely polarizes the electron spin and depolarizes the nuclear spin. Next, we apply a transition selective MW π - x pulse which completely transfers the population of the state $|0,0\rangle$ to $|1,0\rangle$, but leaves the other states unaffected.

Next, we determine the transition frequency of our choice (either $|1,0\rangle \leftrightarrow |1,1\rangle$ or $|1,0\rangle \leftrightarrow |1,-1\rangle$) and apply a RF $\frac{\pi}{2}$ - x pulse with the carrier frequency of the RF pulse equal to this transition frequency. Then, we allow the system to freely evolve for a variable time τ, during which the nuclear spin precesses with a frequency that is offset from the control magnetic field frequency by some amount depending on the interaction of the nuclear spin with its environment (this is identical to the free evolution in an electron spin FID sequence). Next, we apply a RF $\frac{\pi}{2}$ - ϕ pulse (with the carrier frequency equal to the transition frequency), after which we apply another selective MW π - x pulse, which brings back the remaining population in $|1,0\rangle$ to $|0,0\rangle$. Here, $\phi = 2\pi\nu_d\tau$, where ν_d is the detuning frequency (usually set to 20 kHz for our nuclear spin FID experiments) Finally, a readout pulse measures the entire population in the ground state, i.e the sum of the populations in the $|0,0\rangle$, $|0,1\rangle$ and $|0,-1\rangle$ states. The ground state population is plotted against the variable time τ to obtain the FID signal. The complete pulse sequence is shown in Figure 5.4.

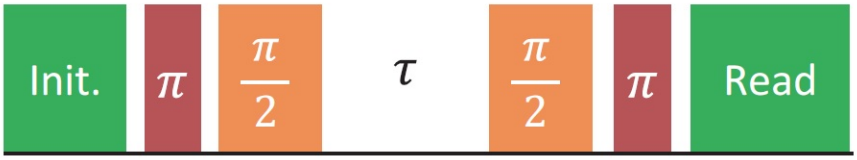

Figure 5.4: The pulse sequence used to measure the nuclear FID signal. The flip angles and phases of both MW_1 pulses are π - x, while the flip angles and phases of the RF_1 pulses are $\frac{\pi}{2}$ - x and $\frac{\pi}{2}$ - ϕ [10].

5.2.2 Experimental implementation

After measuring the nuclear Rabi oscillations using the procedure detailed in Section 5.1.2, we determine the RF $\frac{\pi}{2}$ pulse duration, which we use for the nuclear spin FID experiments to obtain the FID signal. The FFT spectrum of this FID signal helps us measure the offset of the peak from the detuning frequency, and thus determine the exact experimental nuclear spin transition frequencies of our system. Figure 5.5 shows an image of the experimental FID signal observed, and its corresponding FFT spectrum. The FID signal envelope appears to be growing instead of decaying owing to environmental noise. We try to nullify this effect by fitting the data to a Gaussian envelope during data processing, which gives us a sharper peak in the FFT spectrum.

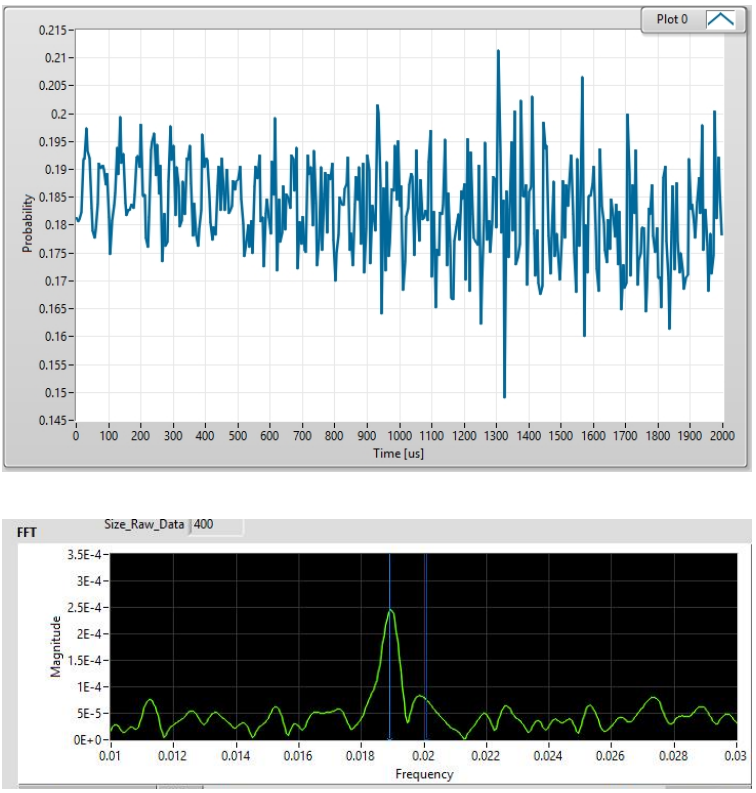

Figure 5.5: An experimental nuclear spin FID signal, and its data-processed FFT spectrum [15].

The major challenge in performing nuclear spin Rabi and FID experiments is the application of the transition selective MW pulse which has to be applied for a long duration, as a result of which the electron spin significantly decoheres by the end of the experiment. To counter this challenge, we attempt to replace this long transition selective MW pulse by a short MW pulse sequence which achieves the required selective population transfer. This method is explored in section 5.3.

5.3 CNOT-like pulse sequence

To perform the selective transition required in nuclear spin Rabi and FID experiments but in a shorter duration, we replace the transition selective MW π - x pulse with a CNOT-like pulse sequence.

5.3.1 Theory

To perform the CNOT-like operation, we first apply an initialization laser pulse, which completely polarizes the electron spin and depolarizes the nuclear spin. Next, we apply a MW $\frac{\pi}{2}$ - x pulse, followed by a free evolution for a fixed time $\tau = \frac{1}{2A_{\parallel}}$. Next, we apply a MW $\frac{\pi}{2}$ - y pulse. The unitary corresponding to this entire operation is:

$$U_{CNOT} = -\frac{i}{2\sqrt{2}}[\cos(\pi\nu\tau - \tfrac{\pi}{4})(\sigma_z - iI_2) + \cos(\pi\nu\tau + \tfrac{\pi}{4})(\sigma_x + \sigma_y)] \otimes [\sin(\pi A\tau)]I_z$$

$$+\frac{i}{2\sqrt{2}}[\cos(\pi\nu\tau + \tfrac{\pi}{4})(\sigma_z - iI_2) - \cos(\pi\nu\tau - \tfrac{\pi}{4})(\sigma_x + \sigma_y)] \otimes [\cos(\pi A\tau) - 1]I_z^2 + I_3.$$

where $\nu = D + \gamma_e B_{0z} - \nu_{mw}$ is the effective transition frequency of the electron spin in the rotating frame (ν_{mw} is equal to the carrier frequency of the MW $\frac{\pi}{2}$ - x and $\frac{\pi}{2}$ - y pulse). When we set the free precession time $\tau = \frac{1}{2A_{\parallel}}$ and $\nu_{mw} = D + \gamma_e B_{0z} - \frac{A_{\parallel}}{2}$, the population in the states $|0,1\rangle$ and $|0,-1\rangle$ get completely transferred to the states $|-1,1\rangle$ and $|-1,-1\rangle$ respectively. When we set the free precession time $\tau = \frac{1}{2A_{\parallel}}$ and $\nu_{mw} = D + \gamma_e B_{0z} + \frac{A_{\parallel}}{2}$, the population in the state $|0,0\rangle$ gets completely transferred to the state $|-1,0\rangle$ (this resembles a CNOT operation up to a global phase factor). To confirm the population transfer, we apply an electron FID MW pulse sequence (with the carrier frequencies of both MW pulses equal to the transition frequency $= D + \gamma_e B_{0z}$) with a variable free evolution time t after the CNOT-like pulse sequence and measure the signal using the readout pulse. The complete pulse sequence is shown in Figure 5.6. The observed FFT spectra after a simple FID MW pulse sequence, and after a CNOT + FID MW pulse sequence (with the carrier frequency of the CNOT-like MW pulses $\nu_{mw} = D + \gamma_e B_{0z} - \frac{A_{\parallel}}{2}$ and $\nu_{mw} = D + \gamma_e B_{0z} + \frac{A_{\parallel}}{2}$) are shown in Figure 5.7. For $\nu_{mw} = D + \gamma_e B_{0z} - \frac{A_{\parallel}}{2}$, the peaks in the FFT spectrum corresponding to $m_n = 1$ and $m_n = -1$ (first and third peaks) are flipped, signifying the complete population transfer of these states. For $\nu_{mw} = D + \gamma_e B_{0z} + \frac{A_{\parallel}}{2}$, the peaks corresponding to $m_n = 0$ (second peak) is flipped, signifying the complete population transfer of this state.

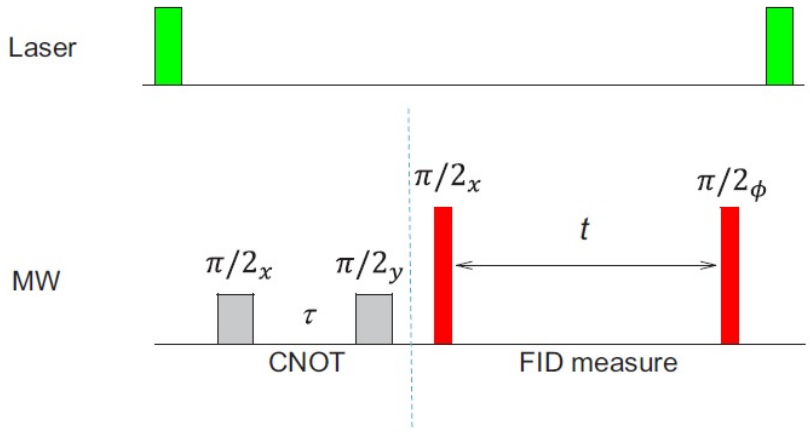

Figure 5.6: The complete CNOT + FID pulse sequence [12].

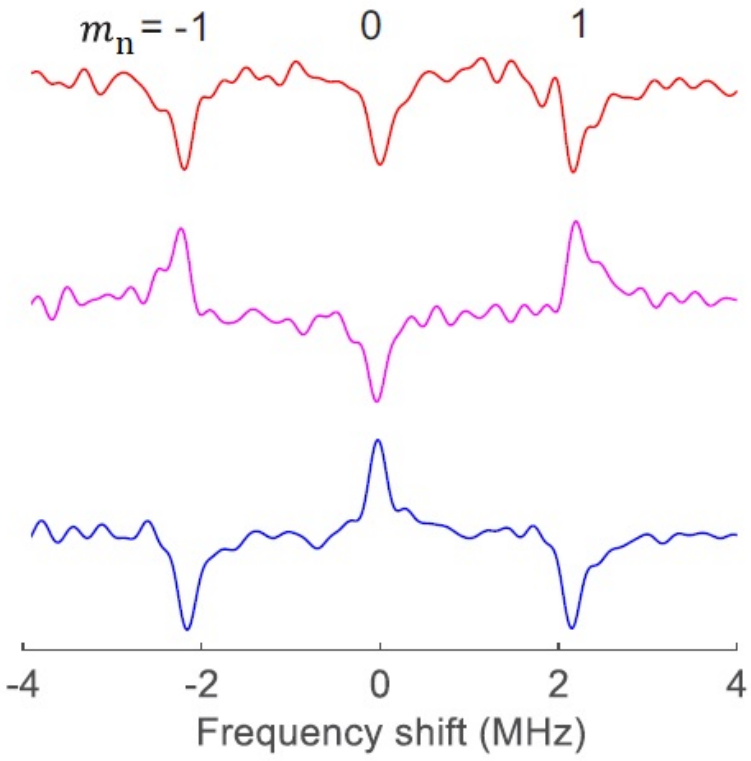

Figure 5.7: The FFT spectrum for a simple FID, a CNOT + FID with the carrier frequency of the CNOT-like pulses $= D + \gamma_e B - \frac{A_\parallel}{2}$, and a CNOT + FID with the carrier frequency of the CNOT-like pulses $= D + \gamma_e B + \frac{A_\parallel}{2}$ [12].

5.3.2 Experimental Implementation

After choosing an NV center and the $m_s = 0 \leftrightarrow m_s =$ -1 transition, we determine the MW π and $\frac{\pi}{2}$ pulse durations by measuring the electron Rabi oscillations. Next, we apply the CNOT + FID MW pulse sequence with the phases, carrier frequencies and durations of the pulses as mentioned in section 5.3.1.

As a small caveat, I had coded such a pulse sequence consisting of 4 pulses and 5 delays using C++, and interfaced it to the AWG of our setup.

Ideally, the fixed time $\tau = \frac{1}{2A_{\parallel}} \approx 231$ ns, since $A_{\parallel}$ for a two spin system consisting of an electron and a ^{14}N nuclear spin is 2.16 MHz. We varied τ from 210 to 250 ns to determine the best value of τ for our experimental implementations, and the best value of τ for both CNOT-like pulses was found to be around 230 ns. The results of the experimentally obtained FFT spectrum of the CNOT + FID pulse sequence (as well as it's comparision to the FFT spectrum of the FID pulse sequence after global phase correction) are shown in Figure 5.8. The first spectrum in Figure 5.8, with the carrier frequency of the CNOT-like pulses equal to $D + \gamma_e B - \frac{A_{\parallel}}{2}$ has the first and third peaks (corresponding to $m_n = +1$ and $m_n =$ -1) flipped, while the second spectrum, with the carrier frequency of the CNOT-like pulses equal to $D + \gamma_e B + \frac{A_{\parallel}}{2}$ has the second peak (corresponding to $m_n = 0$) flipped. The duration of the entire CNOT-like MW pulse sequence is around 300 ns, while the duration of a transition selective MW pulse is around 1200 ns. Therfore, the CNOT-like MW pulse sequence performs the same operation as the transition selective MW pulse (for the $m_s = 0 \leftrightarrow m_s =$ -1 subspace), but in a much shorter duration.

Towards the end of my project, we will substitute the transition selective MW π - x pulse in the nuclear spin Rabi and FID pulse sequences with this CNOT-like pulse sequence, and check if we can obtain better results of nuclear Rabi oscillations and the nuclear FID signal.

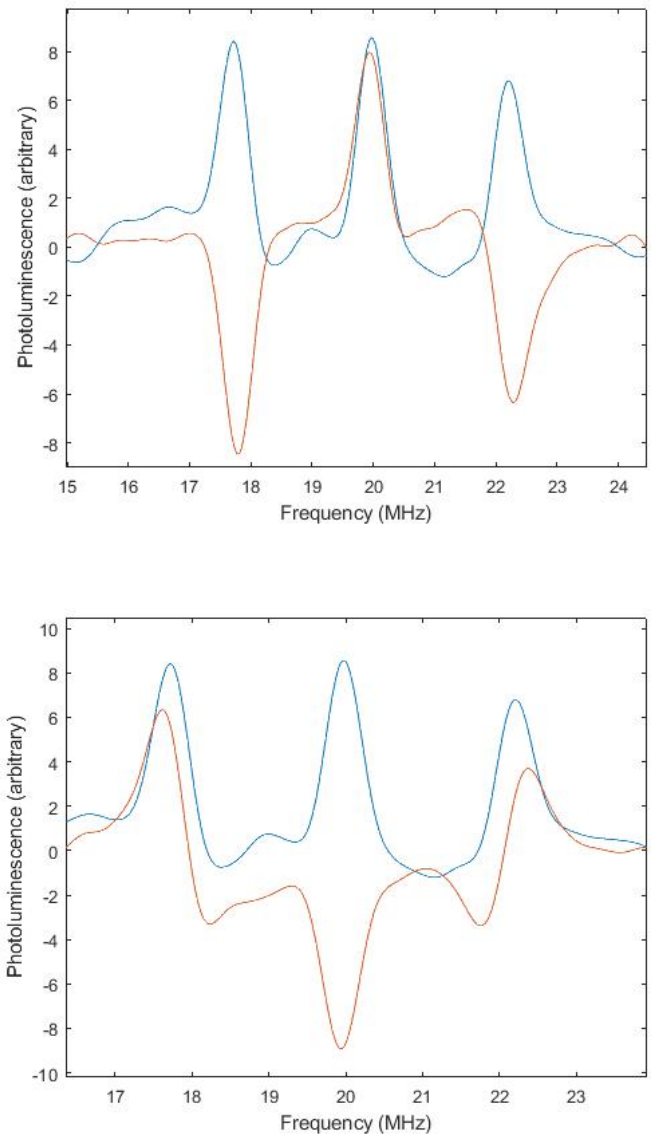

Figure 5.8: A comparison of the FFT spectrum of the signal observed after a CNOT+FID pulse sequence with carrier frequency $= D + \gamma_e B - \frac{A_\parallel}{2}$ and $D + \gamma_e B - \frac{A_\parallel}{2}$ respectively, with the FFT spectrum of an FID signal [15].

Chapter 6

Conclusion

In this thesis, we explored the theoretical effect and experimental implementation of various spin control techniques for both the electron as well as nuclear spins in NV centers. We started with the theoretical Hamiltonian characterization of a spin in the NV center, which is imperative to performing spin control experiments. We talked about the different components present in an NV setup, and the experimental challenges one needs to overcome before starting spin control experiments. Some aspects of the spin control experiments, including some of the theoretical details and a summary of some of the steps involved in performing these experiments has been detailed in this thesis. We also explored some of the challenges associated with performing optimal spin control experiments, and detailed a method to overcome one of these challenges.

This research can be built upon to perform more advanced spin control experiments, using more complicated pulse sequences. These pulse sequences can easily be applied by coding them and interfacing the sequences with the AWG of the setup, as had been done in our experiments. The control of both electron and nuclear spins opens up the avenue to perform multi-qubit experiments, and fully utilise the hybrid nature of NV registers (fast gate operations using electron spins and long-term information storage using nuclear spins).

Another useful experiment, which I was unable to complete during my project, is the interleaving of two qubit gate operations with DD pulses applied on the electron spin, so as to improve the fidelity of the applied gate operation [13].

Bibliography

[1] D. Suter *et al.*, *Single-Spin Magnetic Resonance in the Nitrogen-Vacancy Center of Diamond*, Progress in Nuclear Magnetic Resonance Spectroscopy **98**, pp. 50-62 (2017)

[2] M.W. Doherty *et al.*, *The nitrogen-vacancy colour centre in diamond*, Physics Reports **528(1)**, 1-45 (2013)

[3] L.M.K. Vandersypen *et al.*, *NMR techniques for quantum control and computation*, Reviews of Modern Physics **76**, 1037 (2004)

[4] Rotating Wave Approximation, Wikipedia

[5] S. Sangtawesin, *Quantum Control of Nuclear Spins Coupled to Nitrogen-Vacancy Centers in Diamond* [Doctoral Dissertation, Harvard University], (2016)

[6] Schematic : V. Latko, TU Dortmund (2020)

[7] Image : D. Suter, TU Dortmund (2020)

[8] `www.mriquestions.com`

[9] J. Zhang *et al.*, *Fast Quantum State Tomography in the Nitrogen Vacancy Center of Diamond* (manuscript in progress)

[10] J.H. Shim *et al.*, *Room-temperature high-speed nuclear-spin quantum memory in diamond*, Phys. Rev. A **87**, 012301 (2013)

[11] H. Levitt, *Spin dynamics: basics of nuclear magnetic resonance*, John Wiley &. Sons, Ltd. (2001)

[12] J. Zhang *et al.*, *Pulse sequences for controlled two and three-qubit gates in a hybrid quantum register*, Phys. Rev. A **98**, 042302 (2018)

[13] J. Zhang *et al.*, *Experimental Protection of Two-Qubit Quantum Gates against Environmental Noise by Dynamical Decoupling*, Phys. Rev. Letters **115**, 110502 (2015)

[14] K.R.K. Rao *et al.*, *Characterization of hyperfine interaction between an NV electron spin and a first-shell ^{13}C nuclear spin in diamond*, Phys. Rev. B **94**, 060101 (2016)

[15] \\StorageE3\User\E3a\Research_Data\NV\Projects\
Rounak_Thesis_data